JOC The Journal of Organic Chemistry

pubs.acs.org/joc Article

Synthesis, Protonation and Aromatic Characteristics of a Series of 1,10-Phenanthroline-Fused Porphyrinoids

Victoria C. Ujah, Deyaa I. AbuSalim, and Timothy D. Lash*

Cite This: J. Org. Chem. 2025, 90, 8−29 Read Online

ACCESS | Metrics & More | Article Recommendations | Supporting Information

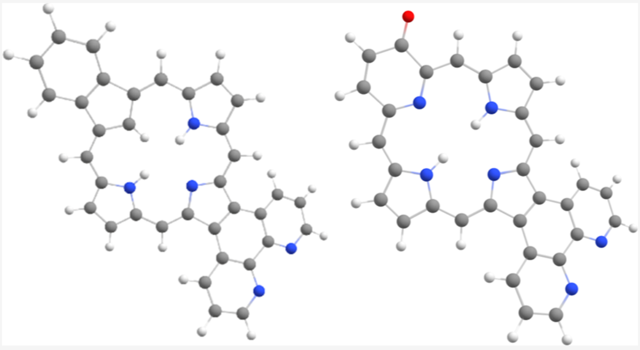

ABSTRACT: A series of porphyrin analogues with fused 1,10-phenanthroline units were synthesized. The proton NMR spectra for phenanthroline-fused heteroporphyrins showed significantly upfield shifted *meso*-proton resonances compared to related porphyrinoid systems and the peaks corresponding to alkyl substituents directly attached to these macrocycles were also observed further upfield. These results indicate that the presence of the phenanthroline unit leads to reduced diatropicity, but the internal NH resonance was also further upfield, a result that is inconsistent with this interpretation. A phenanthrene-fused carbaporphyrin gave an unexpectedly upfield singlet for the internal C−H at nearly −9 ppm, while the NH protons appeared at −6.8 ppm. These unusual chemical shifts again imply enhanced diatropicity but the reduced downfield shifts for the external protons indicates that the aromatic ring current has been significantly reduced. Similar results were obtained for phenanthroline-fused oxybenzi- and oxypyriporphyrins. Detailed analyses of the spectroscopic properties for these systems are reported and protonation studies were conducted. The conjugation pathways and aromatic properties were computationally analyzed using nucleus independent chemical shifts (NICS) and anisotropy of induced current density plots.

INTRODUCTION

Porphyrin chemistry continues to be an intriguing area of research. Initially, the biological significance of metalloporphyrin pigments such as heme and chlorophyll provided the chief impetus for these studies,[1,2] but the field subsequently diversified due in part to potential applications in many different areas including catalysis,[3] sensor development,[4] optical materials,[5] and medicine.[6] In relation to the latter area, the possibility of using porphyrins as photosensitizers in photodynamic therapy has received widespread attention.[7] This in turn encouraged investigations into modified porphyrin-like systems (porphyrinoids) that have altered, potentially enhanced, properties. One approach to porphyrinoids with altered characteristics involves core modification where one or more of the internal nitrogen atoms have been replaced with O, S, Se or C (structures **1a**−**c** and **2**)[8,9] or further modified subunits such as the ones present in oxypyriporphyrins **3** and oxybenziporphyrins **4** (Figure 1).[9,10] Many of these systems retain porphyrin-type aromaticity, although nonaromatic or antiaromatic structures have also been reported.[11,12]

Another strategy to modify the porphyrin system involves the introduction of fused rings that alter or extend the conjugation pathways.[13] In a recent study, a series of tropone-fused porphyrinoids **5**−**8** (Figure 2) were prepared that showed greatly modified characteristics.[14] Although tropone-fused porphyrin **5** only gave a slightly altered electronic absorption

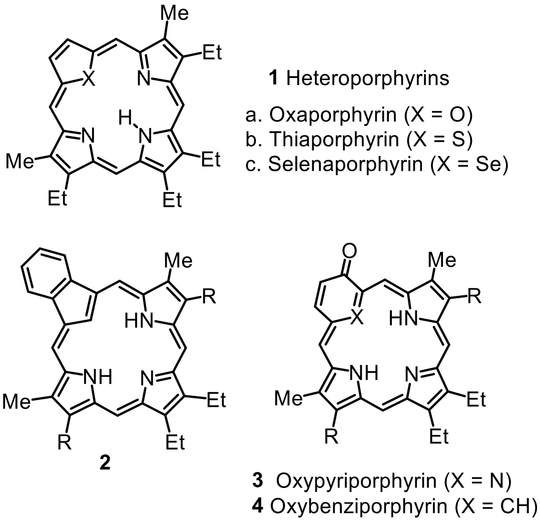

Figure 1. Examples of porphyrin analogues.

Received: June 15, 2024
Revised: September 7, 2024
Accepted: December 4, 2024
Published: December 12, 2024

https://doi.org/10.1021/acs.joc.4c01511
J. Org. Chem. 2025, 90, 8−29

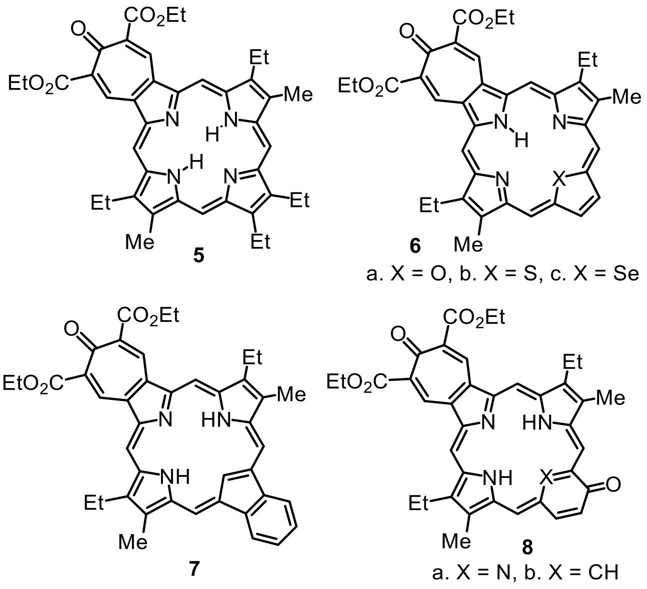

Figure 2. Tropone-fused porphyrinoids.

spectrum with a bathochromically shifted Soret band at 439 nm, the proton NMR spectrum showed unexpectedly upfield shifts to the *meso*-protons, from a typical value of 10 ppm, to give two 2H singlets at 9.56 and 9.13 ppm. These values suggest that the macrocyclic ring current has been significantly reduced. However, this result was seemingly contradicted by the relatively upfield shift to the NH resonance, which appeared at −5.32 ppm, a value that is indicative of increased diatropicity. The related heteroporphyrins **6a**−**c** showed similar effects, but much larger changes were noted for carbaporphyrin **7**, oxypyriporphyrin **8a** and oxybenziporphyrin **8b**.[14] For instance, the *meso*-proton resonances for benzocarbaporphyrins **2** without fused tropone units appear at approximately 10 ppm, while the internal CH is usually present near −6.8 ppm. In the proton NMR spectrum for **7** in $CDCl_3$, the *meso*-proton resonances showed up as two 2H singlets at 9.04 and 8.50 ppm, while the inner CH appeared at −9.29 ppm.[14] Although these values showed small variations with concentration and temperature, the strong upfield shifts to both the internal and external protons are difficult to reconcile.

In order to gain a better understanding of this phenomenon, alternative annulated porphyrinoids showing similar effects were sought. The tropone unit in **5**−**8** is electron-withdrawing and we speculated that similar effects might accrue from the presence of other fused electron-deficient units. In fact, electron-withdrawing substituents are known to diminish the aromatic character of porphyrins and related macrocycles.[15,16] In earlier work, we had investigated the synthesis of porphyrins **9** with fused 1,10-phenanthroline units using an efficient "3 + 1" variant on the MacDonald condensation (Scheme 1).[17,18] This system was later shown to form interesting ruthenium(II) complexes[19] but phenanthrolinoporphyrins have otherwise not been extensively studied. In this work, a series of phenanthrolinoporphyrinoids have been synthesized and the effects of this unit on the spectroscopic properties of the resulting macrocycles have been assessed. In particular, the presence of fused phenanthroline rings is shown to significantly affect the aromatic properties of these derivatives.

■ RESULTS AND DISCUSSION

5-Nitro-1,10-phenanthroline undergoes a Barton-Zard condensation with ethyl isocyanoacetate in the presence of 1,8-diazabicyclo[5.4.0]undec-7-ene (DBU) to give phenanthrolinopyrrole **10** (Scheme 1).[17,18] Cleavage of the ester moiety with KOH in ethylene glycol affords unsubstituted heterocycle **11** and this condenses with two equivalents of acetoxymethylpyrroles **12** in refluxing acetic acid-2-propanol to give the crucial tripyrrane intermediate **13**.[17,18] In previous work, the *tert*-butyl ester protective groups of **13** were cleaved with trifluoroacetic acid, the mixture was diluted with dichloromethane, and the resulting diunsubstituted tripyrrane **14** reacted with pyrrole dialdehyde **15**. Following oxidation with 2,3-dichloro-5,6-dicyano-1,4-benzoquinone (DDQ), column chromatography and recrystallization, phenanthrolinoporphyrins **9** were isolated in 75−83% yield.[17,18] The UV−vis spectra for **9a** and **9b** in chloroform were very similar to the spectra obtained for

Scheme 1. Synthesis of Phenanthrolinoporphyrins

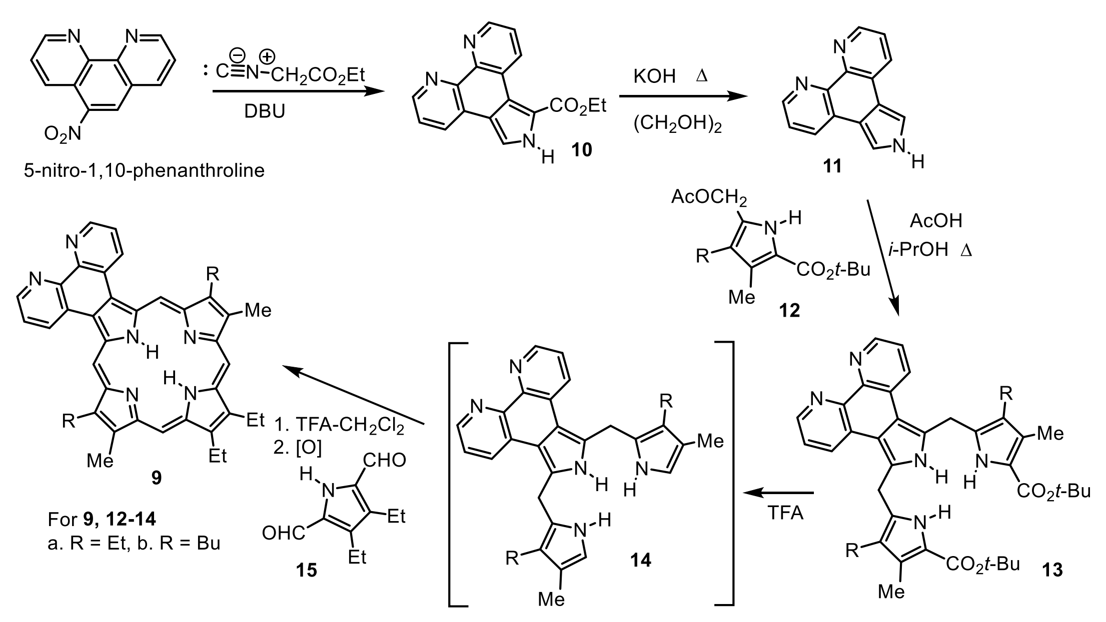

structurally related phenanthroporphyrins such as **16** (Figure 3)[20] giving rise to a Soret band at 424 nm and weaker Q bands at 522, 562, 582, and 636 nm. In the original work, the reported NMR spectra were obtained in TFA-$CDCl_3$,[18] but a proton NMR spectrum of free base **9b** in $CDCl_3$ has now been obtained at 55 °C. This gave two 2H singlets for the *meso*-protons at 10.14 and 9.49 ppm, while the internal. NH protons afforded a broad peak at −4.07 ppm. This contrasts to phenanthroporphyrin **16** (Figure 3) which showed the *meso*-proton resonances at 11.03 and 10.03 ppm and the NH protons at −3.60 ppm.[20] Both the internal and external protons in **9b** were shifted upfield compared to the analogous phenanthroporphyrin, but the results must be treated with caution because significant shifts may result from changes in temperature and concentration. Nevertheless, the spectra tentatively indicate that the phenomenon observed for tropone-fused porphyrinoids may also apply to phenanthrolinoporphyrins **9**.

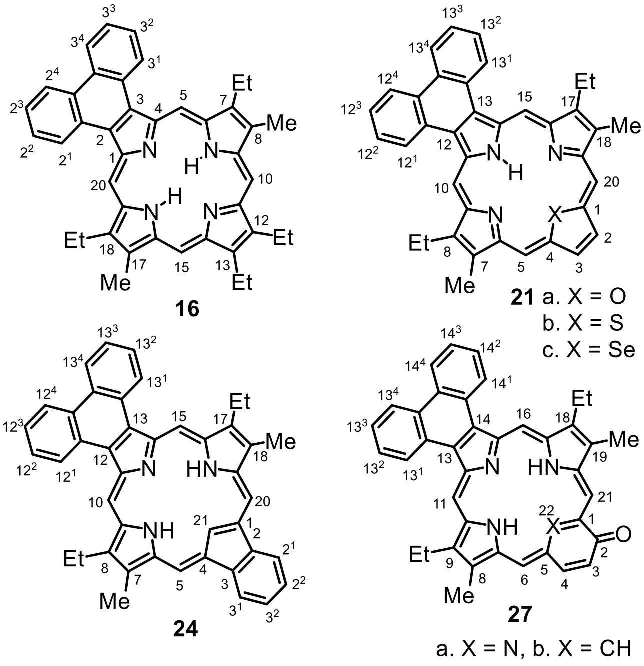

Figure 3. Selected phenanthrene-fused porphyrinoids.

Additional insights can be obtained by comparing the proton NMR chemical shifts for 1,10-phenanthroline[21] and phenanthrolinopyrrole **11** with the equivalent phenanthroline protons in porphyrin **9b** (Table 1). Although the phenanthroline protons directly adjacent to the porphyrin macrocycle (**c**) are strongly deshielded by the macrocyclic ring current, protons of type **a** and **b** are further removed and are more informative. In phenanthrolinopyrrole **11**, protons **a** and **b** are shielded compared to 1,10-phenanthroline, and these shifts can be attributed to electron-donation from the electron-rich pyrrole moiety. In porphyrin **9b**, the equivalent protons are shifted downfield indicating that the fused heterocycle takes part in global aromatic conjugation pathways. Similar effects can be seen in related phenanthroline-fused porphyrinoids (Table 1).

In order to better understanding of these effects, a series of heteroporphyrins **17**−**19** were prepared (Scheme 2). Tripyrrane **13b** was deprotected with TFA, condensed with furan dialdehyde **20a** and oxidized with DDQ to afford oxaporphyrin **17** in 44−87% yield. Unfortunately, oxaporphyrin **17** was virtually insoluble in chloroform and this prevented us from obtaining a proton NMR spectrum for the free base. As is the case for other oxaporphyrins,[22] **17** was easily protonated. Attempts to obtain the UV−vis spectrum for **17** in deacidified dichloromethane gave rise to a spectrum corresponding to a mixture of the free base and a protonated species. However, the free base spectrum could be obtained in 1% triethylamine-dichloromethane (Figure 4). The spectrum exhibited a broad and relatively weak Soret band at 418 nm and a series of Q bands between 500 and 670 nm. Initial protonation of the system is observed in the presence of 1−2 equiv of TFA in CH_2Cl_2 and the new species gave a much stronger Soret band at 409 nm and Q bands at 552, 569, and 593 nm. In this case, computational analysis (vide infra) indicates that internal protonation leads to monocation **17′**H^+ rather than the externally protonated species **17**H^+ (Scheme 3). At much higher concentrations of TFA, a third species was identified, and these results were tentatively attributed to the formation of an externally protonated structure **17**H_2^{2+} rather than the doubly core protonated species **17′**H_2^{2+}. The results are similar to those obtained for phenanthrooxaporphyrin **21a** (Figure 3),[20] which was monoprotonated in

Table 1. Proton NMR Chemical Shifts for the Equivalent Resonances Observed for 1,10-Phenanthroline, Phenanthrolinopyrrole 11 and Related Porphyrinoids in $CDCl_3$

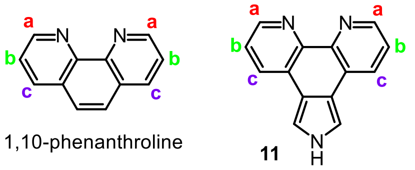

	a	b	c
1,10-phenanthroline[24]	9.13	7.62	8.24
11[20]	8.96	7.48	8.33
9b	9.40	7.86	9.70
18	9.40	7.74−7.72	9.33
19	9.42	7.73	9.32−9.28
23	9.37	7.72−7.69	9.01
26	9.46, 9.43	7.89, 7.85	9.18, 9.02
28	9.40, 9.39	7.76, 7.70	8.99, 8.77

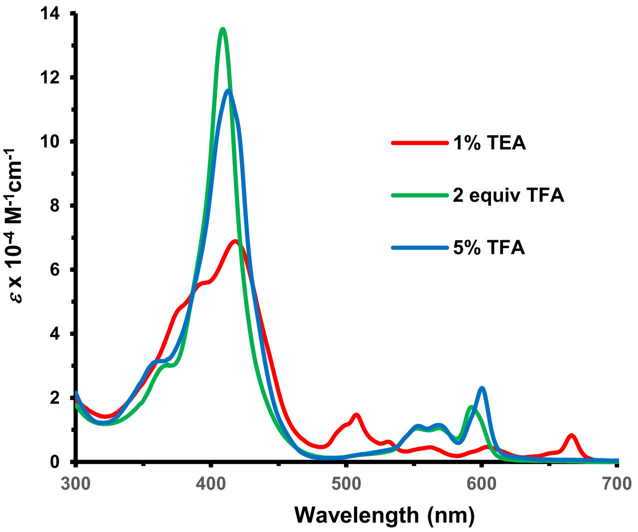

Figure 4. UV−vis spectra for oxaporphyrin **17** in 1% Et_3N−CH_2Cl_2 (red line), in CH_2Cl_2 with 2 equiv of TFA (green line) and in 5% TFA-CH_2Cl_2 (blue line).

Scheme 2. Synthesis of a Series of Porphyrinoids with Fused 1,10-Phenanthroline Units

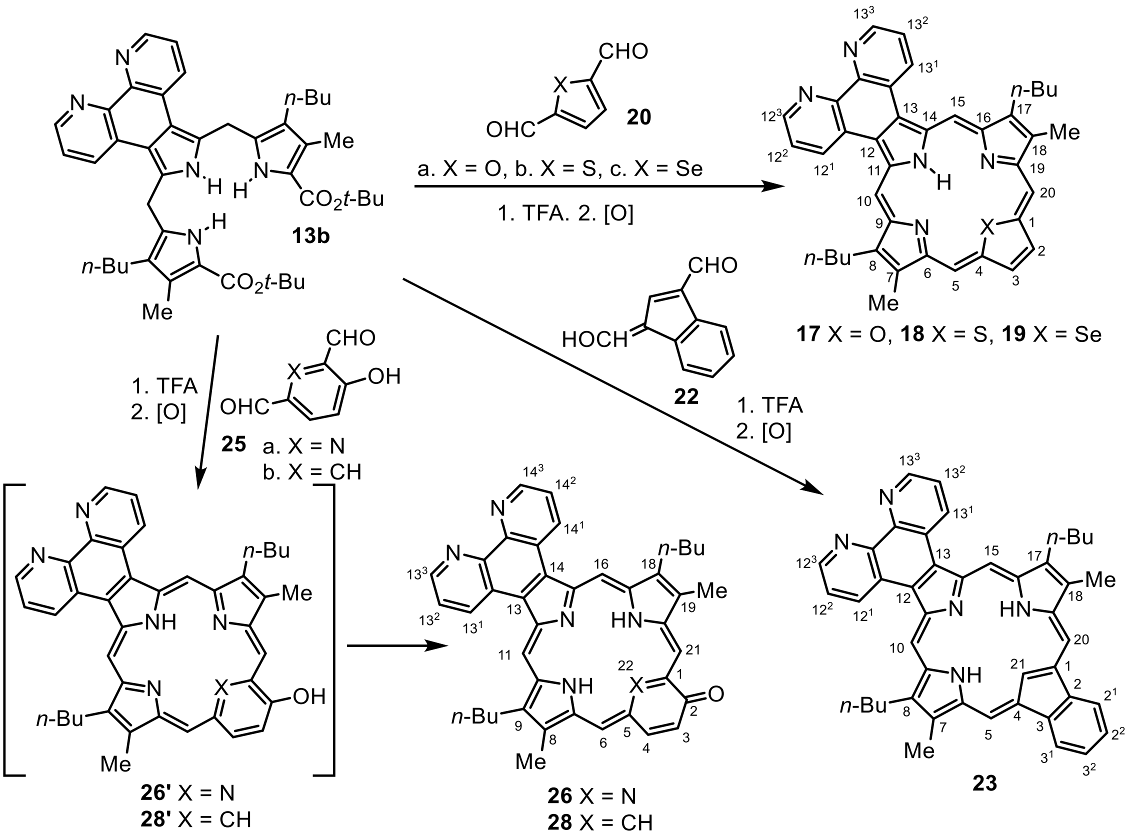

the presence of trace amounts of TFA but only underwent diprotonation at very high concentrations of TFA, although diprotonation of **21a** must take place within the porphyrinoid core. In 10% TFA-CH_2Cl_2, **17** gave a broadened, slightly bathochromically shifted Soret band, followed by Q bands at 553, 569, and 600 nm. It is worth noting that phenanthroline is weakly basic ($pK_a = 4.86$)[23] and while it competes with core protonation in many phenanthrolinoporphyrinoid systems (vide supra), oxaporphyrins appear to have considerably higher basicity. On the other hand, diprotonation of 1,10-phenanthroline is not favored. NMR data for **17** could be obtained in TFA-$CDCl_3$ and the protonated species produced strongly deshielded *meso*-proton resonances at 11.59 and 11.08 ppm, while the internal NH resonance appeared at −5.09 ppm. The carbon-13 NMR spectrum showed the *meso*-carbons at 97.9 and 105.3 ppm and demonstrated that the macrocycle possesses a plane of symmetry. The data are consistent with a strongly aromatic porphyrinoid cation.

Reaction of tripyrrane **13b** with thiophene dialdehyde **20b** afforded phenanthrolinothiaporphyrin **18** in 79% yield (Scheme 2). The proton NMR spectrum was consistent with a strongly aromatic porphyrinoid but showed upfield shifts to both the external and internal protons compared to the analogous phenanthrothiaporphyrin **21b**[20] (Table 2). The *meso*-protons for **21b** appeared at 11.15 and 10.67 ppm but shifted to 9.80 and 10.42 ppm in phenanthrolinothiaporphyrin **18** (Table 2 and Figure 5). Importantly, the protons adjacent to the phenanthroline unit, labeled a in Table 2, were shifted upfield to a substantial degree (1.35 ppm) but the *meso*-protons flanking the thiophene ring (b) only moved upfield by 0.25 ppm. Although the NH resonance for **21b** appeared at −3.21 ppm, this moved upfield by >1 ppm in **18**. These results cannot easily be interpreted but on balance the diatropicity in **18** appears to be reduced compared to **21b**. For many porphyrinoids, the macrocyclic ring current is so large that directly attached alkyl substituents are also strongly deshielded.[24] Methyl substituents commonly give rise to singlets near 3.6 ppm and the chemical shift for this unit provides an alternative measure of the aromatic ring current. Therefore, it is worth noting that the methyl resonance for **21b** appears at 3.45 ppm but in **18** this peak is shifted upfield to 3.25 ppm (Table 2). However, the phenanthroline resonances are significantly shifted downfield in **9b** and phenanthrolinothiaporphyrin **18** (Table 1) and this provides support for the presence of extended aromatic pathways in this system.

The UV−vis spectrum for **18** is very porphyrin-like, showing a strong Soret band at 424 nm and a series of Q bands between 500 and 680 nm (Figure 6). Spectroscopic titration with up to 20 equiv of trifluoroacetic acid gave a new species with an intensified Soret band at 425 nm, and Q bands at 571 and 613 nm, that was attributed to the formation of a monoprotonated structure. Unlike oxaporphyrins **17**, computational results show that external protonation to give **18**H^+ is slightly favored compared to the internally protonated form **18′**H^+ (Scheme 3). Addition of larger amounts of TFA, up to 1000 equiv of TFA, shifted the Soret band to 431 nm and the longest wavelength Q-band to 617 nm. This appears to result from a second protonation to give dications such as **18**H_2^{2+}.

Condensation of **13b** with selenophene dialdehyde **20c** gave selenaporphyrin **19** in 55% yield. The UV−vis spectrum for **19** in CH_2Cl_2 gave a strong Soret band at 421 nm and Q bands at 520, 559, 579, and 633 nm (Figure 7). Addition of up to 50 equiv of TFA led to the formation of a protonated species attributed to **19**H^+ that gave a weakened Soret band at 434 nm and weaker absorptions at 523, 584, 630, and 688 nm. Further addition of up

Scheme 3. Protonation of Phenanthroline-Fused Heteroporphyrins

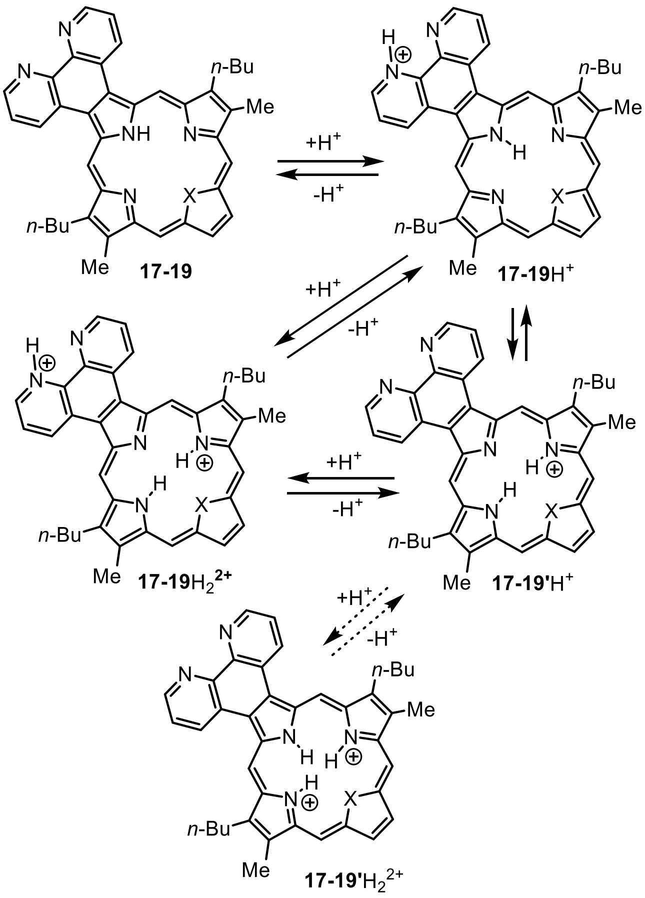

Table 2. Selected Proton NMR Resonances for Phenanthrolinoporphyrin 9b, Thiaporphyrin 18, Selenaporphyrin 19 and Related Phenanthroporphyrinoids 16, 21b and 21c

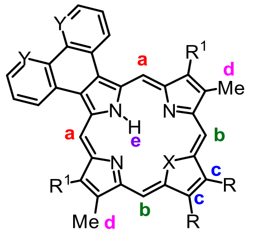

9b X = NH, Y = N, R = Et, R^1 = *n*-Bu
16 X = NH, Y = CH, R = R^1 = Et
18 X = S, Y = N, R = H, R^1 = *n*-Bu
21b X = S, Y = CH, R = H, R^1 = Et
19 X = Se, Y = N, R = H, R^1 = *n*-Bu
21c X = Se, Y = CH, R = H, R^1 = Et

	a	b	c	d	e
9b	10.14	9.49		3.52	−4.07
16[23]	11.03	10.03		3.68	−3.60
18	9.80	10.42	9.96	3.25	−4.49
21b[23]	11.15	10.67	10.08	3.45	−3.21
19[a]	9.78	10.55	10.24	3.22	−4.81
19	10.08	10.60	10.26	3.27	−4.38
21c[23]	11.28	10.87	10.41	3.47	−3.40

[a] Proton NMR spectrum obtained in $CDCl_3$ at 29 °C; all the other NMR spectra were run at 55 °C.

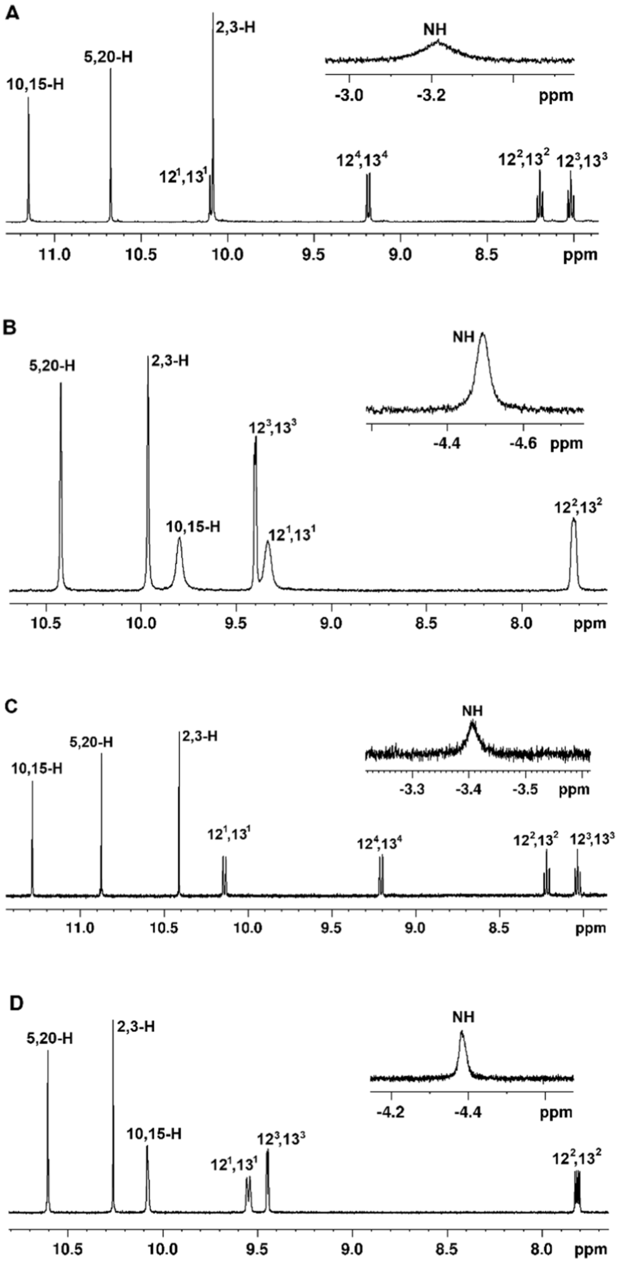

Figure 5. Partial proton NMR spectra of phenanthrothiaporphyrin **21b** (A), phenanthrolinothiaporphyrin **18** (B), phenanthroselenaporphyrin **21c** (C) and phenanthrolinoselenaporphyrin **19** (D) in $CDCl_3$ at 55 °C showing details of the upfield and downfield regions.

to 2000 equiv of TFA led to the formation of a new species with a stronger Soret band at 450 nm and broad Q bands between 550 and 650 nm, and this was assigned to the formation of dications such as $\mathbf{19}H_2^{2+}$ (Scheme 3). At even higher concentrations of TFA, the Soret band was diminished but the appearance of the spectrum was otherwise only slightly modified. A comparison of the proton NMR spectrum for **19** in $CDCl_3$ at 55 °C with the analogous phenanthrene-fused selenaporphyrin **21c** (Figure 3) showed the same trends noted above for thiaporphyrins **18** and **21b** (Figure 5 and Table 2). The *meso*-protons for **21c** appeared at 11.28 and 10.87 ppm, compared to 10.08 and 10.60 ppm for the corresponding resonances in **19**. The selenophene protons also moved upfield by 0.15 ppm, and the methyl resonances were similarly shifted upfield from 3.47 to 3.27 ppm. All of these results point to diminished diatropicity in the phenanthroline-fused porphyrinoid, but this is contradicted by the interior NH resonance being shifted upfield by nearly 1 ppm going from **21c** to **19**. It should be noted that these differences were even larger when the spectrum was run at 29 °C (Table 2), once again

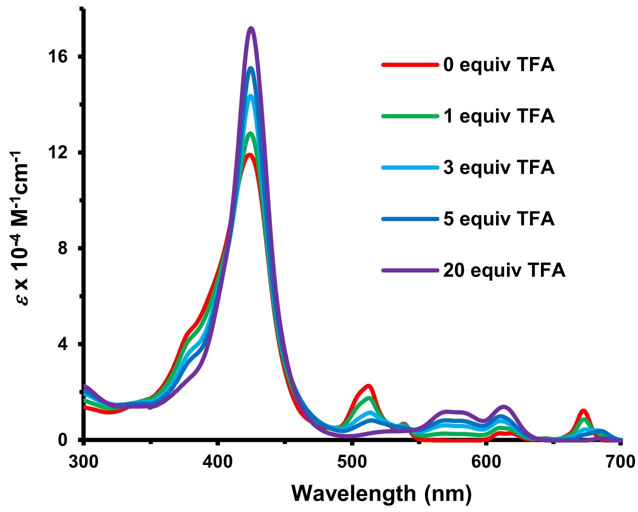

Figure 6. UV−vis spectra of thiaporphyrin **18** in CH_2Cl_2 with 0−20 equiv of TFA.

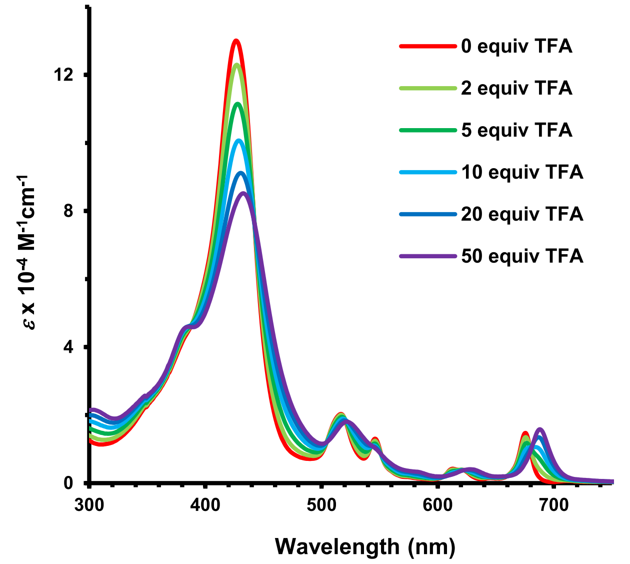

Figure 7. UV−vis spectra of selenaporphyrin **19** in CH_2Cl_2 with 0−50 equiv of TFA.

demonstrating that temperature is a factor in determining the chemical shifts for these systems. However, the phenanthroline protons in **19** are deshielded compared to 1,10-phenanthroline (Table 1), as was the case for **9b** and **18**, indicating that the diatropic pathways extend through the fused heterocycle.

Density functional theory (DFT) calculations[25−28] were carried out on a series of phenanthroline-fused porphyrinoid tautomers and related protonated species. The structures were optimized using M06-2X with the triple-ζ basis set 6-311++G(d,p). Four tautomers of unsubstituted phenanthrolinoporphyrin (**PP**) were considered and the two forms with opposite N−H protons were shown to have the lowest energies (Table 3). All four structures have moderately planar macrocycles but the phenanthroline unit is significantly twisted (Table S1, Figures S116 and S117). Tautomer **PPb** is slightly more stable than **PPa** but the conjugation pathways showed considerable differences (Table 3). The aromatic character of these structures was assessed using nucleus independent chemical shift (NICS) calculations.[29] Standard NICS calculations include effects due to σ and π electrons and are not always accurate. In this work, NICS(0) and NICS$(1)_{zz}$ calculations were carried out. In NICS$(1)_{zz}$, the calculations were performed 1 Å above the ring and the results provide a more accurate measure of the diatropic ring currents. Negative values correspond to aromatic species, while positive values are obtained for antiaromatic systems. Positive values may also be observed when the NICS values are measured at points that are external to the aromatic delocalization pathways. All four tautomers gave strongly aromatic NICS(0) and NICS$(1)_{zz}$ values (Table 3). The NICS$_{zz}$ values are much larger than those for standard NICS calculations but otherwise the observed trends were similar. The porphyrinoid structures were also assessed using anisotropy of induced current density (AICD).[30] The AICD plot for **PPa** indicates that a significant 30π electron diatropic circuit is present that extends around the periphery of the fused phenanthroline unit but the standard porphyrin-type 18π electron delocalization pathway is favored for **PPb** (Figure 8). However, the NICS and NICS$_{zz}$ values for the individual rings in these structures are similar and rings e and g in the phenanthroline subunit do not show a significant increase for **PPa** compared to **PPb** even though the AICD plots point toward the presence of an extended aromatic pathway.

When considering monoprotonated phenanthrolinoporphyrins (**PP**H$^+$), the computational results show that initial protonation is favored on the phenanthroline unit to give **PPe**H$^+$ (Table 4). The data confirms that the system retains a strongly aromatic ring current. **PPa**H$^+$, **PPb**H$^+$ and **PPc**H$^+$ are distorted due to crowding within the porphyrin cavity but apart from the twisted fused phenanthroline unit, the more favored structures **PPd**H$^+$ and **PPe**H$^+$ are nearly planar (Table S1 and Figure S118). Five diprotonated species were also considered (Table 5) and the most stable tautomer was shown to be **PPc**H_2^{2+} with three internal protons on rings a, b and c, and a single protonation on the fused phenanthroline. Again, all five dications gave strongly negative NICS values.

Free base phenanthrolinoheteroporphyrins were assessed similarly (Table 6). In each case, two tautomers were considered. In each case, the phenanthroline unit is significantly twisted relative to the core macrocycle (Tables S2−S4; Figures S120, S123 and S127). Phenanthrolino-oxaporphyrin (**POx**) favors tautomer **POx−a** with internal N−H situated opposite the oxygen atom. The related phenanthrolinothia- (**PT**) and selenaporphyrins (**PS**) also favor the analogous tautomers **PTa** and **PSa**, respectively (Table 6). The AICD plots for these tautomers show the presence of a dominant aromatic circuit that passes around the periphery of the phenanthroline unit (Figure 9).

In the oxaporphyrin series, monoprotonation is favored within the porphyrinoid cavity (Table S8). The most stable form, **POx−a**H$^+$ places the internal N−H's opposite to one another to facilitate hydrogen bonding interactions, but even the less favored internally protonated form **POx−b**H$^+$ is ca. 5 kcal/mol more stable than externally protonated structures (Figure 10). In the thiaporphyrin series, there is virtually no difference between the internally protonated form **PTa**H$^+$ and phenanthroline-protonated tautomer **PTc**H$^+$. This trend continues for selenaporphyrin cations **PS**H$^+$ as the externally protonated structure **PSc**H$^+$ is now favored by >3 kcal/mol (Table S8, Figure 10). Oxaporphyrins are known to be relatively basic compared to thia- or selenaporphyrins, but crowding within the macrocyclic cavities may also play a role in determining the preferred sites for protonation. For each series, four diproto-

Table 3. Calculated Relative Energies (kcal/mol) and NICS Values for Selected Phenanthrolinoporphyrin Tautomers

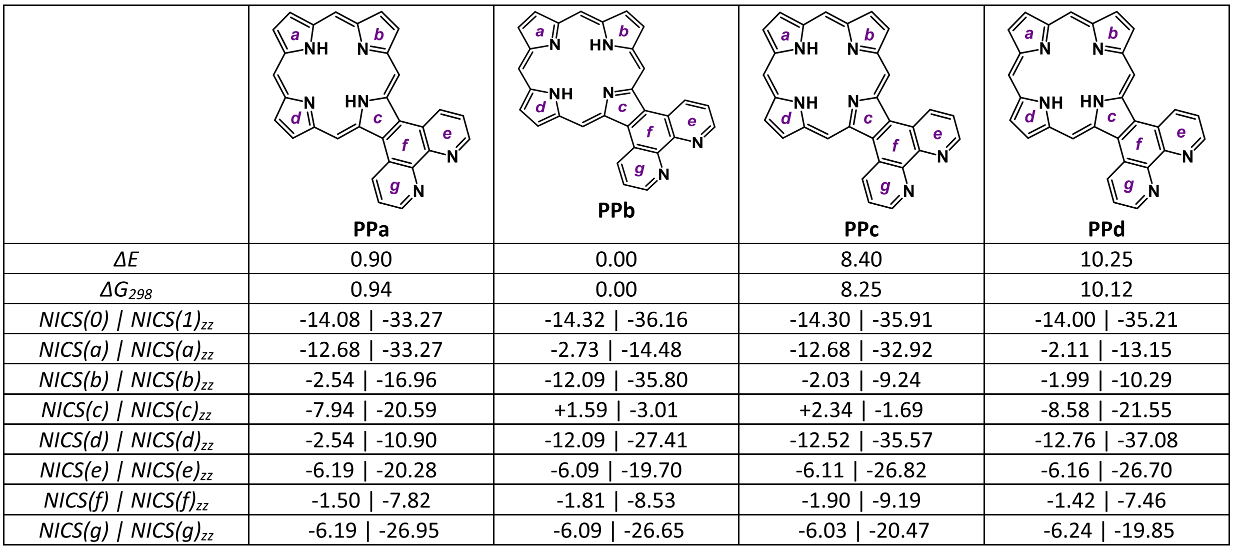

	PPa	PPb	PPc	PPd
ΔE	0.90	0.00	8.40	10.25
ΔG_{298}	0.94	0.00	8.25	10.12
NICS(0) | NICS(1)$_{zz}$	-14.08 | -33.27	-14.32 | -36.16	-14.30 | -35.91	-14.00 | -35.21
NICS(a) | NICS(a)$_{zz}$	-12.68 | -33.27	-2.73 | -14.48	-12.68 | -32.92	-2.11 | -13.15
NICS(b) | NICS(b)$_{zz}$	-2.54 | -16.96	-12.09 | -35.80	-2.03 | -9.24	-1.99 | -10.29
NICS(c) | NICS(c)$_{zz}$	-7.94 | -20.59	+1.59 | -3.01	+2.34 | -1.69	-8.58 | -21.55
NICS(d) | NICS(d)$_{zz}$	-2.54 | -10.90	-12.09 | -27.41	-12.52 | -35.57	-12.76 | -37.08
NICS(e) | NICS(e)$_{zz}$	-6.19 | -20.28	-6.09 | -19.70	-6.11 | -26.82	-6.16 | -26.70
NICS(f) | NICS(f)$_{zz}$	-1.50 | -7.82	-1.81 | -8.53	-1.90 | -9.19	-1.42 | -7.46
NICS(g) | NICS(g)$_{zz}$	-6.19 | -26.95	-6.09 | -26.65	-6.03 | -20.47	-6.24 | -19.85

	PPa	PPb	PPc	PPd
ΔE	0.90	0.00	8.40	10.25
ΔG_{298}	0.94	0.00	8.25	10.12
NICS(0) | NICS(1)$_{zz}$	−14.08 | −33.27	−14.32 | −36.16	−14.30 | −35.91	−14.00 | −35.21
NICS(a) | NICS(a)$_{zz}$	−12.68 | −33.27	−2.73 | −14.48	−12.68 | −32.92	−2.11 | −13.15
NICS(b) | NICS(b)$_{zz}$	−2.54 | −16.96	−12.09 | −35.80	−2.03 | −9.24	−1.99 | −10.29
NICS(c) | NICS(c)$_{zz}$	−7.94 | −20.59	+1.59 | −3.01	+2.34 | −1.69	−8.58 | −21.55
NICS(d) | NICS(d)$_{zz}$	−2.54 | −10.90	−12.09 | −27.41	−12.52 | −35.57	−12.76 | −37.08
NICS(e) | NICS(e)$_{zz}$	−6.19 | −20.28	−6.09 | −19.70	−6.11 | −26.82	−6.16 | −26.70
NICS(f) | NICS(f)$_{zz}$	−1.50 | −7.82	−1.81 | −8.53	−1.90 | −9.19	−1.42 | −7.46
NICS(g) | NICS(g)$_{zz}$	−6.19 | −26.95	−6.09 | −26.65	−6.03 | −20.47	−6.24 | −19.85

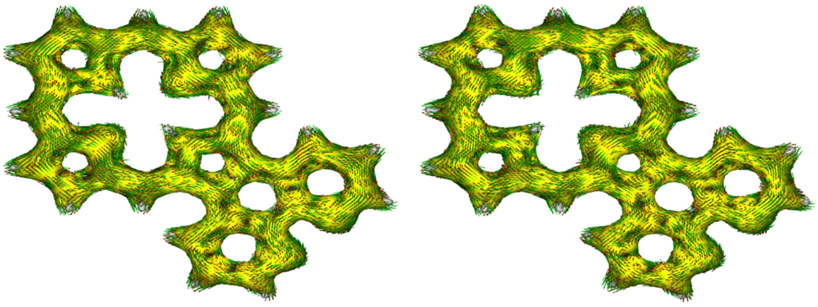

Figure 8. AICD plots (isovalues 0.05) of phenanthrolinoporphyrin tautomers **PPa** (left) and **PPb** (right) showing extension of the aromatic circuits through the fused phenanthrolene rings.

nated structures were considered and in each case the results show that structures protonated both internally and externally are strongly preferred over double protonation within the inner cavity (Table S9). Nevertheless, all of the fully conjugated mono- and dications examined in these studies retained highly diatropic character (Tables S8 and S9).

Indene dialdehyde **22**[31] condensed with tripyrrane **13b** to give phenanthrolinocarbaporphyrin **23** as dark purple crystals in 47% yield. The proton NMR spectrum for **23** in $CDCl_3$ at 55 °C was intriguing (Figure 11 and Table 7) as the internal CH proton was strongly shifted upfield to almost −9 ppm and the NH protons gave a broad 1H resonance near −7 ppm. This contrasts to benzocarbaporphyrins without fused phenanthroline units, which themselves are strongly aromatic, that show the equivalent resonances at −6.8 and −4 ppm, respectively.[32] The structurally equivalent phenanthrocarbaporphyrin **24** (Table 7) showed these peaks at −4.8 and −7.12 ppm.[32] Although these results would ordinarily imply that **23** has enhanced diatropicity compared to **24**, the two 2H singlets for the *meso*-protons appear at 9.05 and 8.63 ppm, while the analogous signals for **24** show up at 10.36 and 9.77 ppm, providing strong evidence for reduced aromatic character. Once again, these contradictory results are difficult to assess as the observed chemical shifts were dependent on temperature and concentration. Nevertheless, the methyl group resonances provided further support for reduced diatropicity as these show up at ca. 2.9 ppm in **23** compared to 3.46 ppm in **24**. In the presence of a trace amount of TFA, the proton NMR spectrum of **23**H^+ showed the internal CH at −6.14 ppm and the *meso*-protons appeared as two 2H singlets at 10.75 and 10.25 ppm, values that are comparable to other monoprotonated carbaporphyrins.

Table 4. Calculated Relative Energies (kcal/mol) and NICS Values for Selected Monoprotonated Phenanthrolinoporphyrins

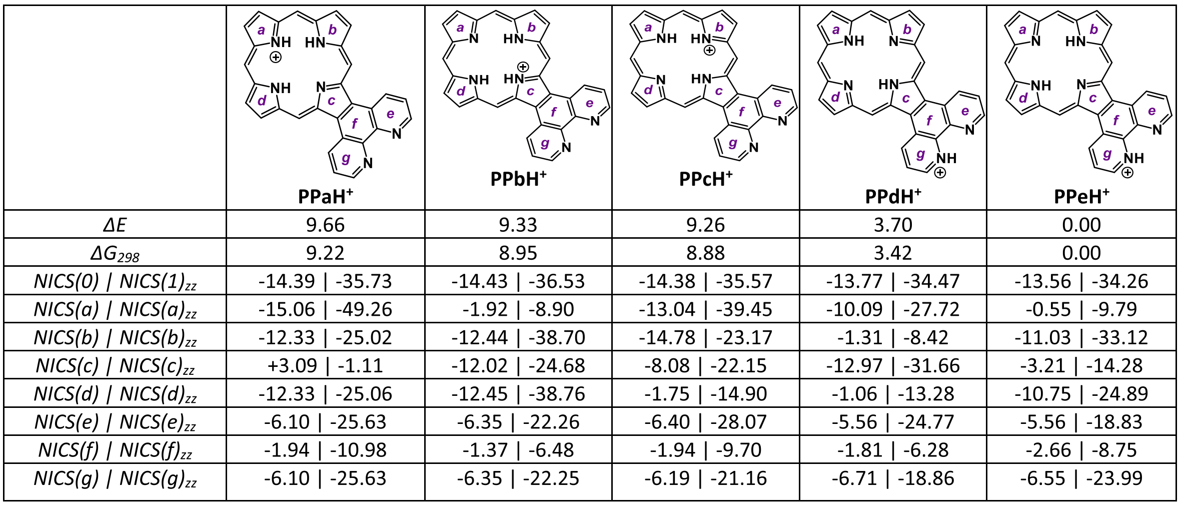

	PPaH$^+$	PPbH$^+$	PPcH$^+$	PPdH$^+$	PPeH$^+$
ΔE	9.66	9.33	9.26	3.70	0.00
ΔG_{298}	9.22	8.95	8.88	3.42	0.00
NICS(0) | NICS(1)$_{zz}$	-14.39 | -35.73	-14.43 | -36.53	-14.38 | -35.57	-13.77 | -34.47	-13.56 | -34.26
NICS(a) | NICS(a)$_{zz}$	-15.06 | -49.26	-1.92 | -8.90	-13.04 | -39.45	-10.09 | -27.72	-0.55 | -9.79
NICS(b) | NICS(b)$_{zz}$	-12.33 | -25.02	-12.44 | -38.70	-14.78 | -23.17	-1.31 | -8.42	-11.03 | -33.12
NICS(c) | NICS(c)$_{zz}$	+3.09 | -1.11	-12.02 | -24.68	-8.08 | -22.15	-12.97 | -31.66	-3.21 | -14.28
NICS(d) | NICS(d)$_{zz}$	-12.33 | -25.06	-12.45 | -38.76	-1.75 | -14.90	-1.06 | -13.28	-10.75 | -24.89
NICS(e) | NICS(e)$_{zz}$	-6.10 | -25.63	-6.35 | -22.26	-6.40 | -28.07	-5.56 | -24.77	-5.56 | -18.83
NICS(f) | NICS(f)$_{zz}$	-1.94 | -10.98	-1.37 | -6.48	-1.94 | -9.70	-1.81 | -6.28	-2.66 | -8.75
NICS(g) | NICS(g)$_{zz}$	-6.10 | -25.63	-6.35 | -22.25	-6.19 | -21.16	-6.71 | -18.86	-6.55 | -23.99

	PPaH$^+$	PPbH$^+$	PPcH$^+$	PPdH$^+$	PPeH$^+$
ΔE	9.66	9.33	9.26	3.70	0.00
ΔG_{298}	9.22	8.95	8.88	3.42	0.00
NICS(0) | NICS(1)$_{zz}$	−14.39 | −35.73	−14.43 | −36.53	−14.38 | −35.57	−13.77 | −34.47	−13.56 | −34.26
NICS(a) | NICS(a)$_{zz}$	−15.06 | −49.26	−1.92 | −8.90	−13.04 | −39.45	−10.09 | −27.72	−0.55 | −9.79
NICS(b) | NICS(b)$_{zz}$	−12.33 | −25.02	−12.44 | −38.70	−14.78 | −23.17	−1.31 | −8.42	−11.03 | −33.12
NICS(c) | NICS(c)$_{zz}$	+3.09 | −1.11	−12.02 | −24.68	−8.08 | −22.15	−12.97 | −31.66	−3.21 | −14.28
NICS(d) | NICS(d)$_{zz}$	−12.33 | −25.06	−12.45 | −38.76	−1.75 | −14.90	−1.06 | −13.28	−10.75 | −24.89
NICS(e) | NICS(e)$_{zz}$	−6.10 | −25.63	−6.35 | −22.26	−6.40 | −28.07	−5.56 | −24.77	−5.56 | −18.83
NICS(f) | NICS(f)$_{zz}$	−1.94 | −10.98	−1.37 | −6.48	−1.94 | −9.70	−1.81 | −6.28	−2.66 | −8.75
NICS(g) | NICS(g)$_{zz}$	−6.10 | −25.63	−6.35 | −22.25	−6.19 | −21.16	−6.71 | −18.86	−6.55 | −23.99

Table 5. Calculated Relative Energies (kcal/mol) and NICS Values for Selected Diprotonated Phenanthrolinoporphyrins

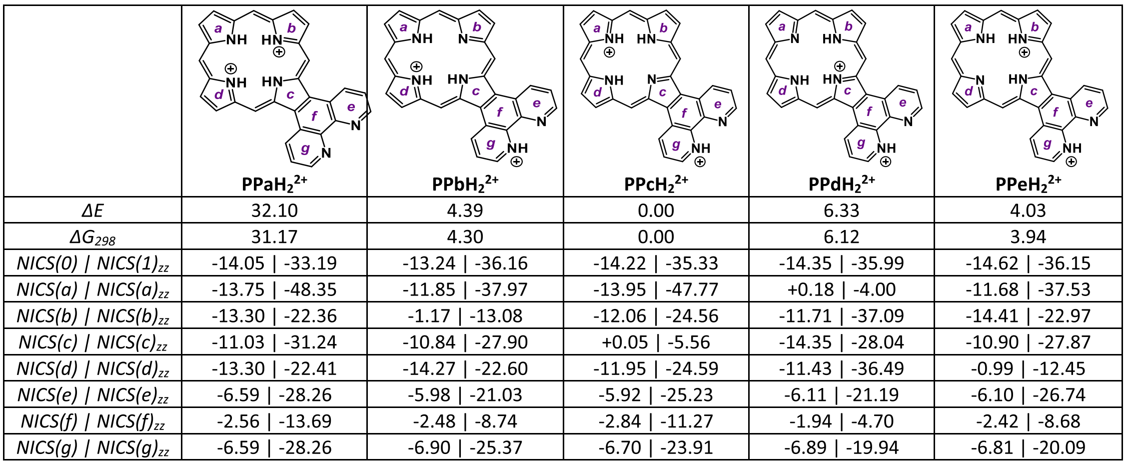

	PPaH$_2^{2+}$	PPbH$_2^{2+}$	PPcH$_2^{2+}$	PPdH$_2^{2+}$	PPeH$_2^{2+}$
ΔE	32.10	4.39	0.00	6.33	4.03
ΔG_{298}	31.17	4.30	0.00	6.12	3.94
NICS(0) | NICS(1)$_{zz}$	-14.05 | -33.19	-13.24 | -36.16	-14.22 | -35.33	-14.35 | -35.99	-14.62 | -36.15
NICS(a) | NICS(a)$_{zz}$	-13.75 | -48.35	-11.85 | -37.97	-13.95 | -47.77	+0.18 | -4.00	-11.68 | -37.53
NICS(b) | NICS(b)$_{zz}$	-13.30 | -22.36	-1.17 | -13.08	-12.06 | -24.56	-11.71 | -37.09	-14.41 | -22.97
NICS(c) | NICS(c)$_{zz}$	-11.03 | -31.24	-10.84 | -27.90	+0.05 | -5.56	-14.35 | -28.04	-10.90 | -27.87
NICS(d) | NICS(d)$_{zz}$	-13.30 | -22.41	-14.27 | -22.60	-11.95 | -24.59	-11.43 | -36.49	-0.99 | -12.45
NICS(e) | NICS(e)$_{zz}$	-6.59 | -28.26	-5.98 | -21.03	-5.92 | -25.23	-6.11 | -21.19	-6.10 | -26.74
NICS(f) | NICS(f)$_{zz}$	-2.56 | -13.69	-2.48 | -8.74	-2.84 | -11.27	-1.94 | -4.70	-2.42 | -8.68
NICS(g) | NICS(g)$_{zz}$	-6.59 | -28.26	-6.90 | -25.37	-6.70 | -23.91	-6.89 | -19.94	-6.81 | -20.09

	PPaH$_2^{2+}$	PPbH$_2^{2+}$	PPcH$_2^{2+}$	PPdH$_2^{2+}$	PPeH$_2^{2+}$
ΔE	32.10	4.39	0.00	6.33	4.03
ΔG_{298}	31.17	4.30	0.00	6.12	3.94
NICS(0) | NICS(1)$_{zz}$	−14.05 | −33.19	−13.24 | −36.16	−14.22 | −35.33	−14.35 | −35.99	−14.62 | −36.15
NICS(a) | NICS(a)$_{zz}$	−13.75 | −48.35	−11.85 | −37.97	−13.95 | −47.77	+0.18 | −4.00	−11.68 | −37.53
NICS(b) | NICS(b)$_{zz}$	−13.30 | −22.36	−1.17 | −13.08	−12.06 | −24.56	−11.71 | −37.09	−14.41 | −22.97
NICS(c) | NICS(c)$_{zz}$	−11.03 | −31.24	−10.84 | −27.90	+0.05 | −5.56	−14.35 | −28.04	−10.90 | −27.87
NICS(d) | NICS(d)$_{zz}$	−13.30 | −22.41	−14.27 | −22.60	−11.95 | −24.59	−11.43 | −36.49	−0.99 | −12.45
NICS(e) | NICS(e)$_{zz}$	−6.59 | −28.26	−5.98 | −21.03	−5.92 | −25.23	−6.11 | −21.19	−6.10 | −26.74
NICS(f) | NICS(f)$_{zz}$	−2.56 | −13.69	−2.48 | −8.74	−2.84 | −11.27	−1.94 | −4.70	−2.42 | −8.68
NICS(g) | NICS(g)$_{zz}$	−6.59 | −28.26	−6.90 | −25.37	−6.70 | −23.91	−6.89 | −19.94	−6.81 | −20.09

The UV–vis spectrum of **23** in CH_2Cl_2 is porphyrin-like, giving a strong Soret band at 444 nm and series of Q bands at 500, 536, 575, and 620 nm (Figure 12). Sequential protonation was observed upon addition of TFA. At approximately 50 equiv

Table 6. Calculated Relative Energies (kcal/mol) and NICS Values for Phenanthrolino-Heteroporphyrin Tautomers

	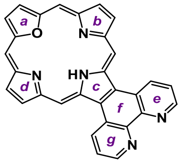 **POx-a**	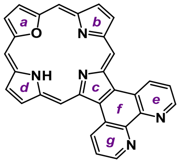 **POx-b**
ΔE	0.00	2.03
ΔG_{298}	0.00	1.57
NICS(0) | NICS(1)$_{zz}$	-14.26 | -35.59	-14.18 | -35.71
NICS(a) | NICS(a)$_{zz}$	-16.47 | -43.62	-16.34 | -42.00
NICS(b) | NICS(b)$_{zz}$	-0.42 | -6.13	+0.76 | -10.35
NICS(c) | NICS(c)$_{zz}$	-7.86 | -20.94	+3.49 | +1.24
NICS(d) | NICS(d)$_{zz}$	-0.42 | -12.75	-12.44 | -29.35
NICS(e) | NICS(e)$_{zz}$	-6.16 | -26.99	-6.09 | -20.35
NICS(f) | NICS(f)$_{zz}$	-1.31 | -7.40	-2.08 | -9.20
NICS(g) | NICS(g)$_{zz}$	-6.16 | -19.93	-6.04 | -26.09

	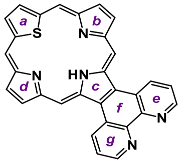 **PTa**	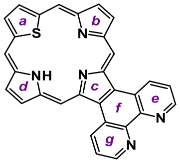 **PTb**
ΔE	0.00	6.46
ΔG_{298}	0.00	6.62
NICS(0) | NICS(1)$_{zz}$	-14.51 | -35.49	-14.36 | -35.53
NICS(a) | NICS(a)$_{zz}$	-16.29 | -38.54	-16.18 | -38.60
NICS(b) | NICS(b)$_{zz}$	-0.84 | -6.10	+0.12 | -12.43
NICS(c) | NICS(c)$_{zz}$	-8.35 | -22.40	+2.43 | -1.42
NICS(d) | NICS(d)$_{zz}$	-0.84 | -6.10	-12.51 | -28.76
NICS(e) | NICS(e)$_{zz}$	-6.16 | -20.23	-6.16 | -19.16
NICS(f) | NICS(f)$_{zz}$	-0.99 | -6.69	-1.68 | -8.09
NICS(g) | NICS(g)$_{zz}$	-6.16 | -19.24	-6.01 | -26.47

	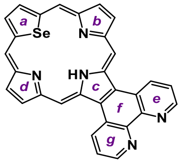 **PSa**	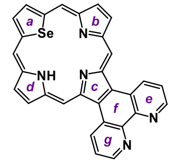 **PSb**
ΔE	0.00	6.46
ΔG_{298}	0.00	6.62
NICS(0) | NICS(1)$_{zz}$	-15.81 | -36.19	-14.66 | -34.99
NICS(a) | NICS(a)$_{zz}$	-14.86 | -34.39	-14.23 | -36.56
NICS(b) | NICS(b)$_{zz}$	-1.25 | -6.54	-0.81 | -16.50
NICS(c) | NICS(c)$_{zz}$	-9.40 | -24.76	+1.73 | -2.52
NICS(d) | NICS(d)$_{zz}$	-1.24 | -14.21	-12.95 | -27.93
NICS(e) | NICS(e)$_{zz}$	-6.13 | -27.13	-6.25 | -19.22
NICS(f) | NICS(f)$_{zz}$	-0.75 | -6.06	-1.69 | -7.84
NICS(g) | NICS(g)$_{zz}$	-6.13 | -19.18	-6.02 | -26.50

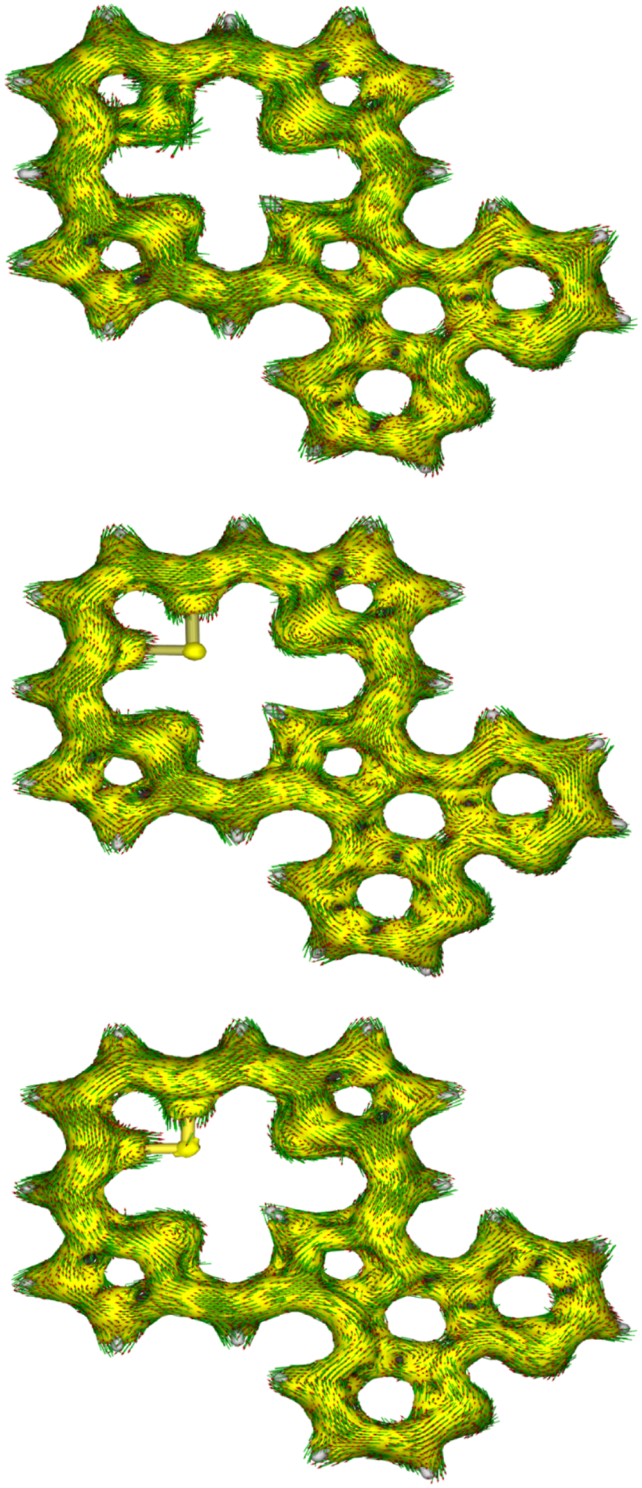

Figure 9. AICD plots (isovalues 0.05) for phenanthrene fused heteroporphyrins **POx−a** (top), **PTa** (middle) and **PSa** (bottom) showing π-extended conjugation pathways.

of TFA, monocation **23**H$^+$ (Scheme 4) was fully formed and this gave a broad weakened Soret band at 453 nm and several broad absorptions between 550 and 750 nm (Figure 12). Although internal and external protonation may occur, computational studies (see below) show that protonation on the phenanthroline unit is favored over monoprotonated species such as **23′**H$^+$. Upon further addition of TFA, a new species emerged and in 1% TFA-CH$_2$Cl$_2$, a Soret band was observed at 472 nm (Figures S20 and S21). This species was attributed to internally protonated dication **23**H$_2^{2+}$. Although carbaporphyrins commonly form C-protonated dications at higher acid concentrations[34] and in this case could potentially produce **23′**H$_2^{2+}$ (Scheme 4), this species is not favored (see below). The UV-spectrum for the dication is bathochromically shifted but otherwise resembles the spectrum for **23**H$^+$. As C-protonation would lead to profound changes in the chromophore, the result

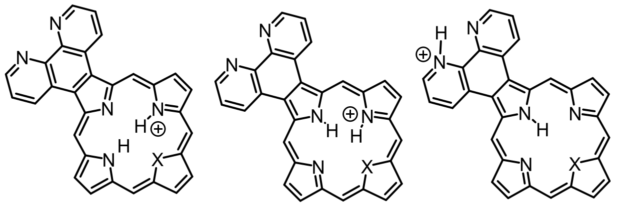

POx-aH$^+$(0.00)
PTaH$^+$(0.19)
PSaH$^+$(3.56)

POx-bH$^+$ (5.10)
PTbH$^+$(2.06)
PSbH$^+$(4.08)

POx-cH$^+$ (11.02)
PTcH$^+$(0.00)
PScH$^+$(0.00)

For **POx-a-c**H$^+$, X = O; **PTa-c**H$^+$, X = S; **PSa-c**H$^+$, X = Se

Figure 10. Selected monoprotonated heterophenanthrolinoporphyrins. Relative energies (ΔE) in kcal/mol are given in parentheses.

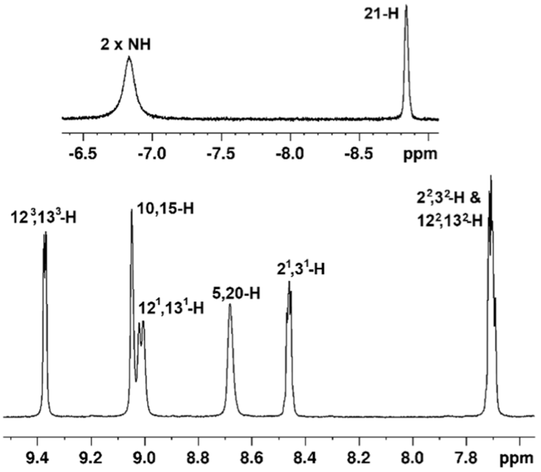

Figure 11. Partial proton NMR spectrum of carbaporphyrin **23** in $CDCl_3$ at 55 °C showing details of the upfield and downfield regions.

Table 7. Selected Proton NMR Resonances for Phenanthrolinocarbaporphyrin 23 and Related Phenanthrocarbaporphyrin 24

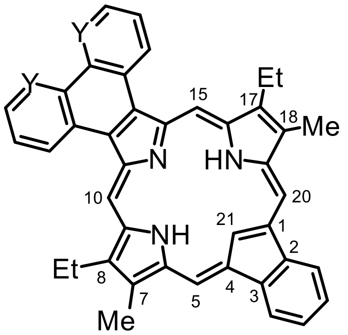

23 Y = N
24 Y - CH

	5,20-H	10,15-H	7,18-Me	NH	21-CH
23	9.05	8.63	2.87	−6.83	−8.84
23[a]	9.41	9.13	2.94	−6.83	−8.75
24[32]	10.36	9.77	3.46	−4.8	−7.12

[a] Proton NMR spectrum obtained at 29 °C; the other NMR spectra were run at 55 °C.

is consistent with the formation of **23**H_2^{2+} (Scheme 4). A new species was formed at higher acid concentrations and in 50% TFA a strong Soret emerged at 451 nm together with two weaker absorptions at 601 and 644 (Figure S22). This was attributed to the formation of C-protonated trication **23**H_3^{3+} (Scheme 4).

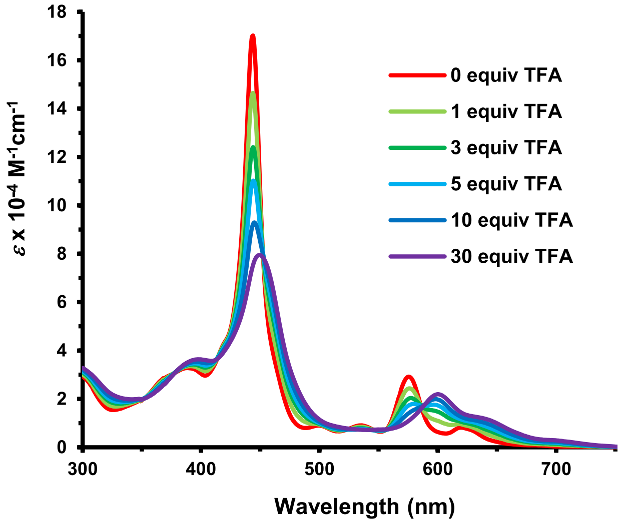

Figure 12. UV−vis spectra of phenanthroline-fused carbaporphyrins **22** in CH_2Cl_2 with 0−30 equiv of TFA.

Scheme 4. Protonation of Phenanthrolinocarbaporphyrin 23

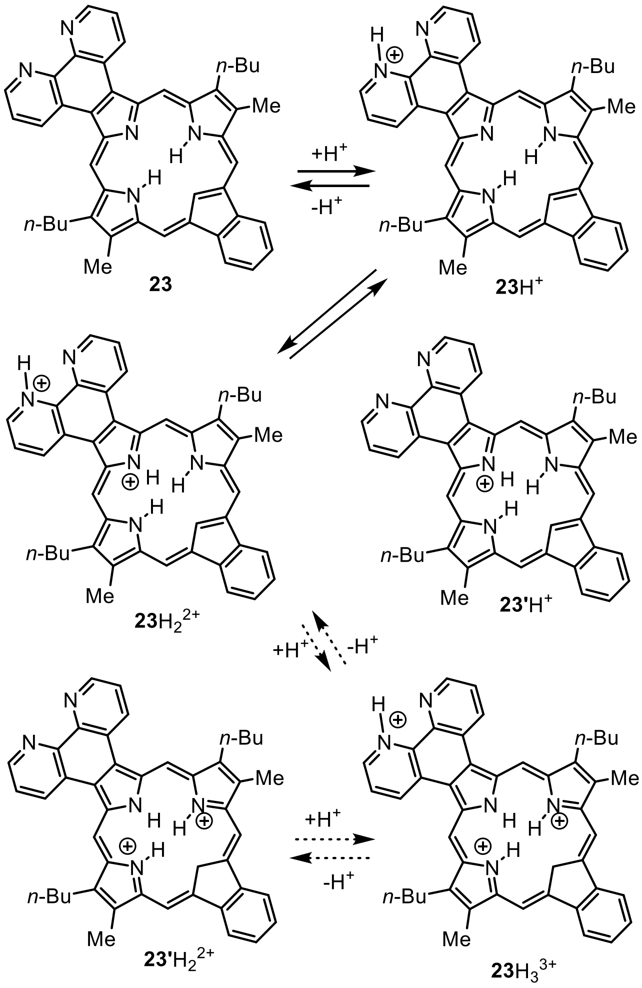

Four fully conjugated tautomers of phenanthrolinobenzocarbaporphyrin (**PBC**) were considered and **PBCa** was shown to be significantly more stable than the other three (Table 8). The more stable tautomers **PBCa** and **PBCb** have crowded cavities and show some loss of planarity and, as is the case for other

Table 8. Calculated Relative Energies (kcal/mol) and NICS Values for Selected Phenanthrolino-Benzocarbaporphyrin Tautomers PBCa−d

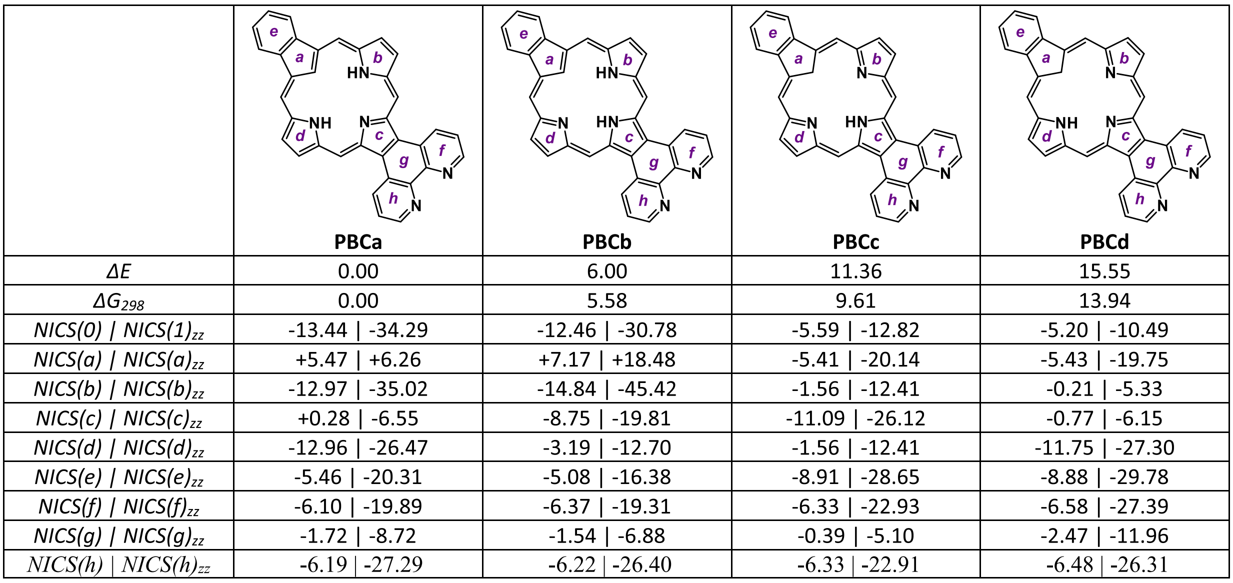

	PBCa	PBCb	PBCc	PBCd
ΔE	0.00	6.00	11.36	15.55
ΔG$_{298}$	0.00	5.58	9.61	13.94
NICS(0) | NICS(1)$_{zz}$	-13.44 | -34.29	-12.46 | -30.78	-5.59 | -12.82	-5.20 | -10.49
NICS(a) | NICS(a)$_{zz}$	+5.47 | +6.26	+7.17 | +18.48	-5.41 | -20.14	-5.43 | -19.75
NICS(b) | NICS(b)$_{zz}$	-12.97 | -35.02	-14.84 | -45.42	-1.56 | -12.41	-0.21 | -5.33
NICS(c) | NICS(c)$_{zz}$	+0.28 | -6.55	-8.75 | -19.81	-11.09 | -26.12	-0.77 | -6.15
NICS(d) | NICS(d)$_{zz}$	-12.96 | -26.47	-3.19 | -12.70	-1.56 | -12.41	-11.75 | -27.30
NICS(e) | NICS(e)$_{zz}$	-5.46 | -20.31	-5.08 | -16.38	-8.91 | -28.65	-8.88 | -29.78
NICS(f) | NICS(f)$_{zz}$	-6.10 | -19.89	-6.37 | -19.31	-6.33 | -22.93	-6.58 | -27.39
NICS(g) | NICS(g)$_{zz}$	-1.72 | -8.72	-1.54 | -6.88	-0.39 | -5.10	-2.47 | -11.96
NICS(h) | NICS(h)$_{zz}$	-6.19 | -27.29	-6.22 | -26.40	-6.33 | -22.91	-6.48 | -26.31

	PBCa	PBCb	PBCc	PBCd
Δ*E*	0.00	6.00	11.36	15.55
Δ*G*$_{298}$	0.00	5.58	9.61	13.94
NICS(0) | NICS(1)$_{zz}$	−13.44 | −34.29	−12.46 | −30.78	−5.59 | −12.82	−5.20 | −10.49
NICS(a) | NICS(a)$_{zz}$	+5.47 | + 6.26	+7.17 | + 18.48	−5.41 | −20.14	−5.43 | −19.75
NICS(b) | NICS(b)$_{zz}$	−12.97 | −35.02	−14.84 | −45.42	−1.56 | −12.41	−0.21 | −5.33
NICS(c) | NICS(c)$_{zz}$	+0.28 | −6.55	−8.75 | −19.81	−11.09 | −26.12	−0.77 | −6.15
NICS(d) | NICS(d)$_{zz}$	−12.96 | −26.47	−3.19 | −12.70	−1.56 | −12.41	−11.75 | −27.30
NICS(e) | NICS(e)$_{zz}$	−5.46 | −20.31	−5.08 | −16.38	−8.91 | −28.65	−8.88 | −29.78
NICS(f) | NICS(f)$_{zz}$	−6.10 | −19.89	−6.37 | −19.31	−6.33 | −22.93	−6.58 | −27.39
NICS(g) | NICS(g)$_{zz}$	−1.72 | −8.72	−1.54 | −6.88	−0.39 | −5.10	−2.47 | −11.96
NICS(h) | NICS(h)$_{zz}$	−6.19 | −27.29	−6.22 | −26.40	−6.33 | −22.91	−6.48 | −26.31

phenanthroline fused porphyrinoids, the phenanthroline unit is strongly twisted relative to the connected pyrrole ring (Table S5 and Figure 13). The preference for **PBCa** over **PBCb** can be attributed, in part, to more favorable hydrogen bonding interactions within the macrocyclic cavity, although NICS calculations suggest that the diatropicity of the former is also slightly higher. C-protonated tautomers **PBCc** and **PBCd** retain some aromatic character but these less stable forms have substantially reduced negative NICS(0) and NICS(1)$_{zz}$ values. The AICD plot of **PBCa** indicates that the conjugation pathways are bifurcated and while the 18π porphyrin-type circuit is favored, a secondary pathway involving the phenanthroline unit is evident (Figure 14). The twisted phenanthroline unit overlies the nearby *meso*-protons (Figure 13) and this appears to be partially responsible for the observed upfield shifts, although this effect can also be discerned for phenanthrene-fused porphyrinoids such as **16**. The same feature affects phenanthrolinoporphyrin **PPa** and related heteroporphyrins. However, this factor does not explain the upfield shifts observed at sites further removed from ring fusion.

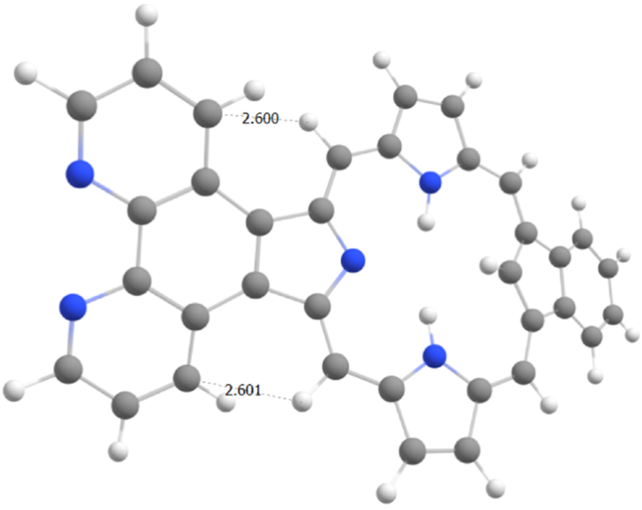

Figure 13. Calculated conformation for favored phenanthroline-fused benzocarbaporphyrin tautomer **PBCa**.

The relative stabilities of potential mono- and diprotonated **PBC** species were investigated. Monoprotonation could give rise to internally or externally protonated species, but externally protonated structure **PBCaH**$^+$ (Figure 15) is by far and away the most stable compared to internally protonated species such as **PBCfH**$^+$ (Table S10). NICS calculations show that all six of the monocations examined are aromatic, although the diatropicity is reduced in C-protonated species (Table S10). The NICS calculations for favored tautomer **PBCaH**$^+$ indicates that an extended pathway running though the periphery of the fused phenanthroline unit predominates (Figure 14), although, as in the case for free base tautomer **PBCa**, the benzo-unit does not

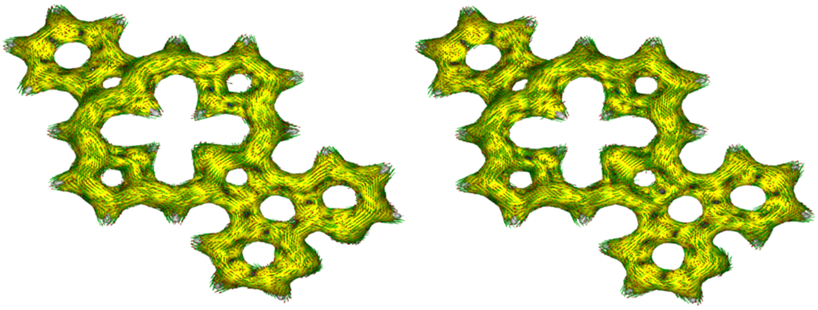

Figure 14. AICD plots of phenanthroline-fused benzocarbaporphyrin **PBCa** and monocation **PBCa**H$^+$ showing the presence of extended diatropic pathways that pass through the phenanthroline unit but not through the benzo-moiety.

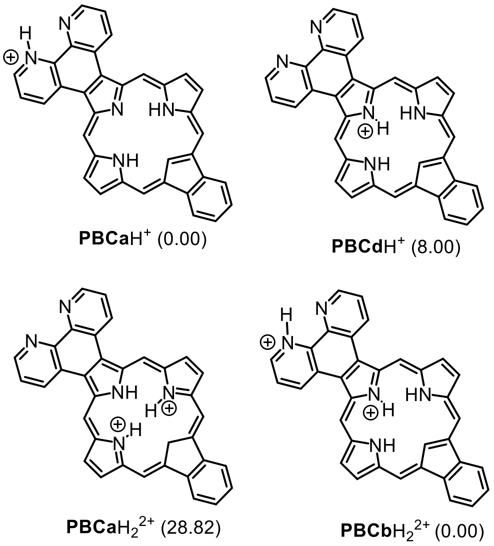

Figure 15. Selected mono- and diprotonated phenanthrolinobenzocarbaporphyrins (PBCs). Relative energies (ΔE) in kcal/mol are given in parentheses.

significantly interact. As expected, diprotonation strongly favors a species **PBCbH$_2$$^{2+}$** with internal and external protonation rather than C-protonated structure **PBCaH$_2$$^{2+}$** (Figure 15 and Table S11).

Although, in principle, the reaction of 4-hydroxy-1,3-pyridinedicarbaldehyde (**25a**) with tripyrrane **13b** could give hydroxypyriphenanthrolinoporphyrin **26′** (Scheme 2), the keto tautomer **26** was favored and could be isolated in 58% yield. As was the case for other phenanthroline-fused porphyrins, oxypyriporphyrin **26** showed anomalously upfield shifts to both the internal and external protons (Table 9 and Figure 16).

Table 9. Selected Proton NMR Resonances for Phenanthrolino-Oxypyriporphyrin 26, Oxybenziporphyrin 28 and Related Phenanthroline-Fused Porphyrinoids 27a and 27b (See Figure 3)

	21-H	*meso*-H	8,19-Me	NH	22-H
26	10.30	8.82, 8.76, 8.49	3.05, 3.01	−6.11, 5.97	
27a[10]	10.59	10.00, 9.98, 9.06	3.45, 3.29	−4.79	
28	9.90	8.97, 8.84, 8.60	3.06, 3.01	−5.4	−7.88
28[a]	9.80	8.73. 8.46, 8.38	2.93, 2.90	−5.73, 5.95	−8.22
27b[10]	10.13	9.74, 9.65, 8.90	3.31, 3.20		−6.90

[a] Proton NMR spectrum obtained at 29 °C; the other NMR spectra were run at 55 °C.

The proton NMR spectrum for **26** in $CDCl_3$ at 55 °C gave four 1H singlets for the *meso*-protons at 10.30, 8.82, 8.76, and 8.49 ppm, while the NH protons gave rise to two peaks near −6 ppm. This contrasts with the related phenanthro-oxypyriporphyrin **27a**[10] (Figure 3) which showed the analogous *meso*-proton resonances at 10.59, 10.00, 9.98, and 9.06 ppm, while the NHs gave a broad peak at −4.79 ppm (Table 9).

The UV−vis spectrum for **26** in CH_2Cl_2 showed the presence of a strong Soret band at 432 nm and Q bands at 601 and 627 nm (Figure 17). Spectrophotometric titration of **26** with trifluoroacetic acid gradually led to the formation of a protonated species, attributed to externally protonated structure **26**H$^+$, although internal protonation could occur to give **26′**H$^+$ (Scheme 5). In the presence of 300 equiv of TFA, the monocationic species gave a broadened diminished Soret band at 436 nm and bathochromically shifted Q bands were observed (Figure 17). Further addition of TFA gave complex results indicative of further protonated species (Figures S25−S28). In 1% TFA-CH_2Cl_2, the Soret band at 434 nm was accompanied by Q bands at 558, 606, 668, and 733 nm. Further changes were noted at higher acid concentrations and in 10% TFA-CH_2Cl_2, an intensified Soret band was observed at 448 nm with Q bands at 582, 615, 675, and 740 nm. Several diprotonated species can be considered (Scheme 5) but the porphyrin-like UV−vis spectrum obtained in 1% TFA-CH_2Cl_2 is not consistent with phenolic species such as **26′**H$_2$$^{2+}$ and **26′**H$_3$$^{3+}$. The spectrum obtained in 10% TFA-CH_2Cl_2 may correspond to a tricationic species such as **26**H$_3$$^{3+}$ (Scheme 5).

DFT calculations confirmed that phenanthrolino-oxypyriporphyrin tautomer **POPa** is favored, although the unusual structure **POPe** is only a little over 4 kcal/mol higher in energy (Table 10). The presence of twisted phenanthroline units was evident in all five tautomers (Table S6 and Figure S134). NICS(0) and NICS(1)$_{zz}$ calculations for **POPa-c** show that these structures are strongly aromatic. Interestingly, **POPe** with its atypical structure has comparable diatropic character. However, not only is hydroxypyridine tautomer **POPd** far less stable, it only possesses weakly diatropic character (Table 10). The AICD plot for **POPa** again shows bifurcated aromatic delocalization pathways with competing 18π electron porphyrin-like circuits and alternative routes passing around the phenanthroline moiety (Figure 18).

Monoprotonation of **POP** is favored on the phenanthroline unit (Table S12) and while resulting tautomer **POPb**H$^+$ (Figure 19) retains comparable diatropic character to free base **POPa**, the AICD plot (Figure 18) clearly shows that the ring current favors an unusual 31-atom route that incorporates the phenanthroline unit. Monoprotonated hydroxypyridine tautomers (Table S12) have greatly reduced global aromatic

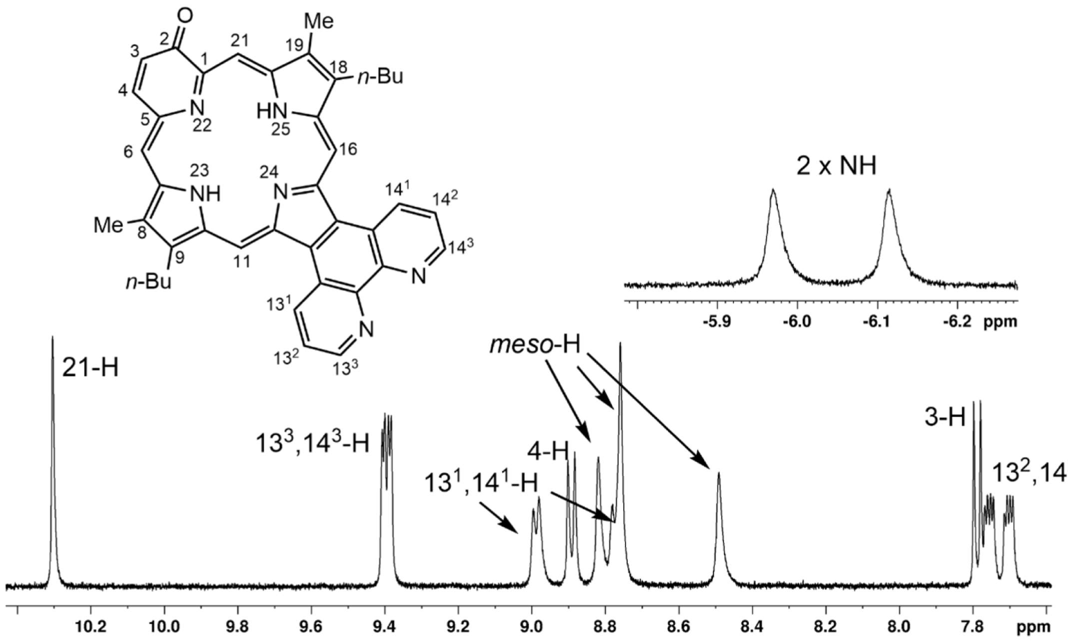

Figure 16. Partial proton NMR spectrum of oxypyriporphyrin **26** in $CDCl_3$ at 55 °C showing details of the upfield and downfield regions.

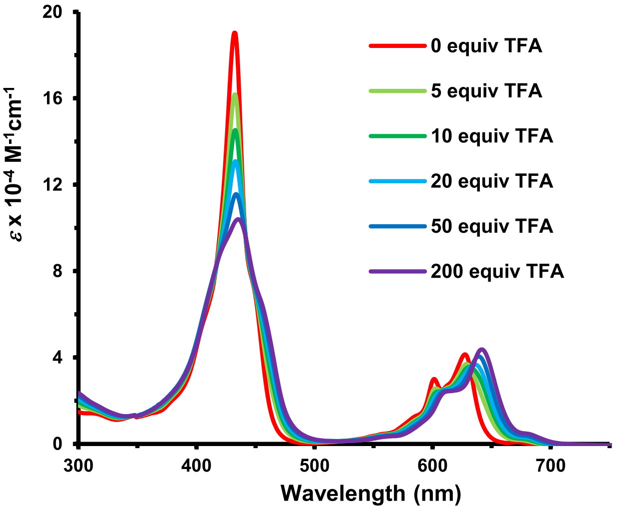

Figure 17. UV−vis spectra of oxypyriporphyrin **26** in CH_2Cl_2 with 0−200 equiv of TFA.

character but **POPfH**$^+$ is only slightly less stable than **POPbH**$^+$ (Figure 19). Seven related dicationic species were investigated and the most stable versions, **POPcH**$_2^{2+}$ and **POPdH**$_2^{2+}$ (Figure 19) proved to be the most stable (Table S13). Even though these tautomers are formally cross-conjugated hydroxypyriporphyrin dications, they retain a significant degree of diatropicity (Table S13).

4-Hydroxy-1,3-benzenedicarbaldehyde (**25b**) was condensed with tripyrrane **13b** to give oxybenziphenanthrolinoporphyrin **28** (Scheme 2). As was the case for oxypyriporphyrin **26**, keto tautomer **28** is favored over phenolic tautomer **28′**. The proton NMR spectrum of oxybenziphenanthrolinoporphyrin **28** in $CDCl_3$ at 55 °C showed the same apparently contradictory results seen for other phenanthroline-fused porphyrinoids (Figure 20). The internal CH was shifted upfield to between −7.88 and −8.22 ppm and the NH protons were seen as two broad peaks between −5.7 and −6.0 ppm (Figure 20). Oxybenziporphyrins **4b** without fused aromatic units give the internal CH resonance at −7.2 ppm, while the NHs give rise to a broad peak near 4.0 ppm.[10] Phenanthrene-fused oxybenziporphyrin **27b** gave a singlet for the inner CH at −6.9 ppm, but the NH resonance could not be identified (Table 9). While these results would ordinarily indicate a greatly increased diamagnetic macrocyclic ring current in **28**, the resonances for the external *meso*-protons tell a different story. Phenanthroporphyrinoid **27b** gave 1H singlets for the *meso*-protons at 10.13, 9.74, 9.65, and 8.90 ppm, but these signals are all shifted upfield in phenanthrolinoporphyrinoid **28** giving singlets at 9.90, 8.97, 8.84, and 8.60 ppm (Table 9). The methyl resonances also imply reduced diatropicity in **28** compared to **27b** as the former gave two 3H singlets at 3.06 and 3.01 ppm, while the latter showed these peaks at 3.31 and 3.20 ppm.

The UV−vis spectrum of **28** in CH_2Cl_2 gave a strong Soret band at 440 nm and Q bands at 624, 666, and 716 nm (Figure 21). This is comparable to oxybenziporphyrin **27b**, which has a strong Soret band at 448 nm and Q bands at 628, 648, and 708 nm.[10] Spectroscopic titration going from 0 to 10 equiv of TFA led to the formation of a protonated species, attributed to monocation **28**H$^+$ (Scheme 5) that was associated with a weakened Soret band and bathochromically shifted Q bands (Figure 21). At higher concentration of TFA further changes were noted and with 1000 equiv of TFA the Soret band appeared at 455 nm and weaker broad absorptions were seen between 600 and 800 nm (Figures S32 and S33). This species could correspond to dications such as **28**H$_2^{2+}$ or **28′**H$_2^{2+}$. In 20% TFA-CH_2Cl_2, a third species emerged with a weakened Soret band at 444 nm (Figure S35) and this may correspond to trication **28**H$_3^{3+}$ (Scheme 5). The proton NMR spectrum of **28** with excess TFA in $CDCl_3$ showed reduced aromaticity as the inner CH appeared near 1.5 ppm, suggesting that this species possesses phenolic character. Interestingly, small spectroscopic changes were noted upon the addition of triethylamine (TEA) to solutions of **28** in CH_2Cl_2. DBU, which is a far stronger base than TEA, had a much larger effect and in 1% DBU-CH_2Cl_2, a new species was identified with three Soret-like bands between 460 and 490 nm and moderately strong Q bands near 700 nm

Scheme 5. Protonation of Phenanthroline-Fused Oxypyri- and Oxybenziporphyrins

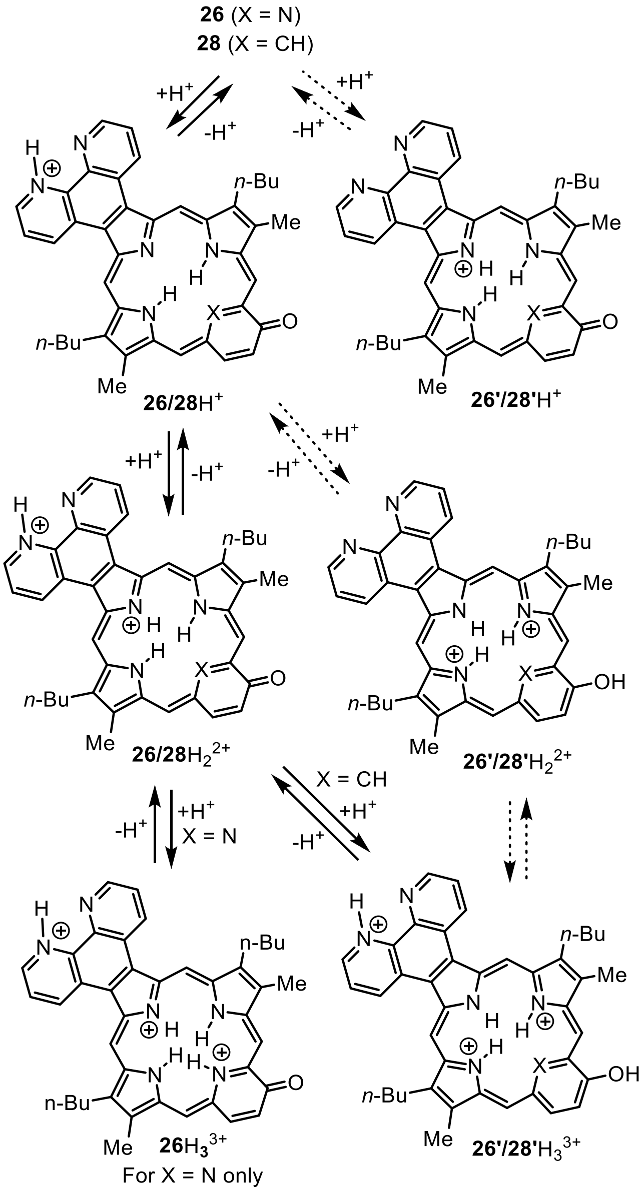

(Figure 22). This species was attributed to deprotonation of **28** to give an anionic species **29** that resembles a conjugated enolate ion (Scheme 6).

As expected, the favored phenanthrolino-oxybenziporphyrin (**POB**) tautomer is **POBa** (Table 11), which possesses a semiquinone unit and N–H protons at opposite positions within the porphyrinoid cavity. **POBb** and **POBc** have core arrangements that are less conducive to hydrogen bonding interactions but **POBa–c** all exhibit global aromatic properties. Once again, the fused phenanthroline units are twisted relative to the macrocyclic core (Table S7 and Figure S138). As was the case for **POPa**, the AICD plot for **POBa** shows that presence of a favored porphyrin-type conjugation pathway together with a secondary circuit that passes through the phenanthroline unit (Figure 23). Hydroxybenziporphyrin **POBd** is a little over 3 kcal/mol less stable than the other three tautomers, due at least in part to the absence of macrocyclic aromaticity (Table 11).

Monoprotonation of **POB** is again favored on the phenanthroline unit (Table S14). For the seven conjugated tautomers considered in this study, **POBb**H$^+$ (Figure 19) proved to be the most stable (Table S14). **POBb**H$^+$ is strongly diatropic and the AICD plot shows the presence of an aromatic circuit that passes through the phenanthroline unit (Figure 23). Internal protonation of the keto form to give **POBa**H$^+$ proved to be >9 kcal/mol less stable (Figure 19). Interestingly, internally protonated phenolic tautomers are far less disfavored (Table S14). In fact, **POBe**H$^+$ (Figure 19) is only just over 3 kcal/mol higher in energy than **POBb**H$^+$. Nevertheless, the aromatic character of hydroxybenziporphyrin tautomers is substantially reduced compared with the keto forms (Table S14). Four diprotonated **POB** structures were considered (Table S15) and moderately aromatic phenolic dications **POBc**H$_2^{2+}$ and **POBd**H$_2^{2+}$ (Figure 19) with internal and external protonations were found to be much more stable than the strongly aromatic keto tautomer (Table S15).

■ CONCLUSIONS

Excellent yields of porphyrinoids fused to 1,10-phenanthroline were obtained by reacting aromatic dialdehydes with a phenanthroline-fused tripyrrane. These porphyrin analogues have unusual spectroscopic properties and the proton NMR spectra showed that both the internal and external proton resonances move upfield compared to the values seen for related structures. The interior NH and CH protons gave peaks between −5 and −9 ppm and this would ordinarily indicate that the macrocycles have greatly increased aromatic character. However, the reduced downfield shifts associated with the external *meso*-protons suggest that these structures have significantly reduced diamagnetic ring currents and this conclusion is supported by the reduced downfield shifts associated with peripheral alkyl substituents. DFT calculations were performed on a series of free base, monoprotonated and diprotonated species and the most favored tautomers were

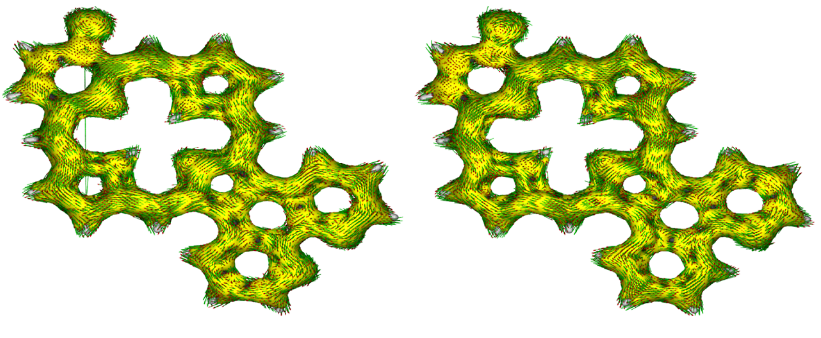

Figure 18. AICD plot (isovalue 0.05) of phenanthroline-fused oxypyriporphyrin **POPa** and monocation **POPb**H$^+$.

Table 10. Calculated Relative Energies (kcal/mol) and NICS Values for Selected Phenanthrolino-Oxypyriporphyrin Tautomers POPa−e

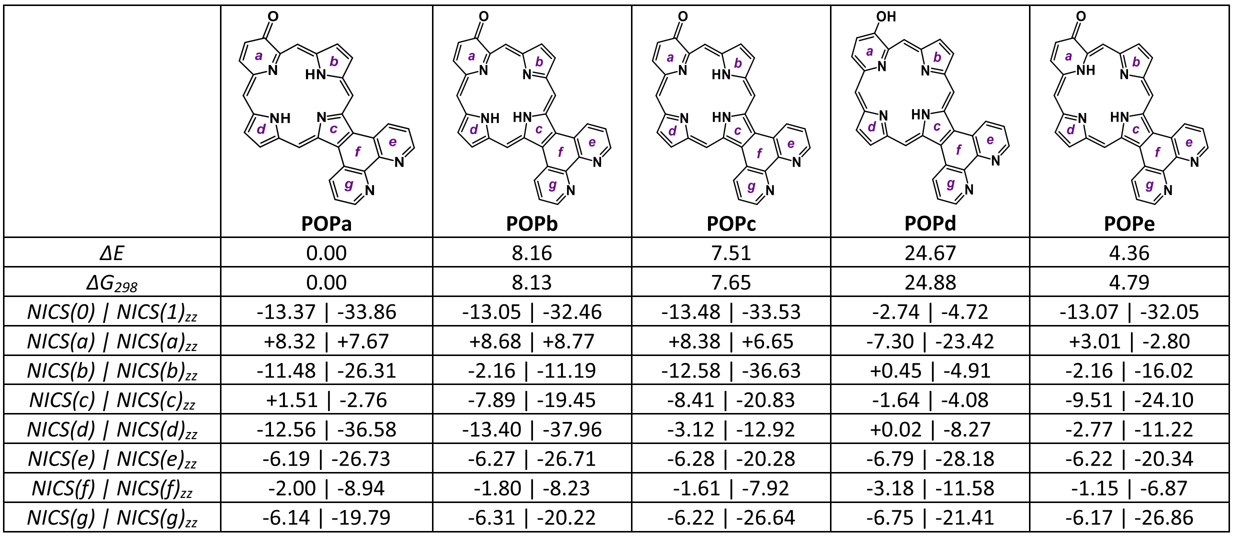

	POPa	POPb	POPc	POPd	POPe
ΔE	0.00	8.16	7.51	24.67	4.36
ΔG_{298}	0.00	8.13	7.65	24.88	4.79
NICS(0) | NICS(1)$_{zz}$	-13.37 | -33.86	-13.05 | -32.46	-13.48 | -33.53	-2.74 | -4.72	-13.07 | -32.05
NICS(a) | NICS(a)$_{zz}$	+8.32 | +7.67	+8.68 | +8.77	+8.38 | +6.65	-7.30 | -23.42	+3.01 | -2.80
NICS(b) | NICS(b)$_{zz}$	-11.48 | -26.31	-2.16 | -11.19	-12.58 | -36.63	+0.45 | -4.91	-2.16 | -16.02
NICS(c) | NICS(c)$_{zz}$	+1.51 | -2.76	-7.89 | -19.45	-8.41 | -20.83	-1.64 | -4.08	-9.51 | -24.10
NICS(d) | NICS(d)$_{zz}$	-12.56 | -36.58	-13.40 | -37.96	-3.12 | -12.92	+0.02 | -8.27	-2.77 | -11.22
NICS(e) | NICS(e)$_{zz}$	-6.19 | -26.73	-6.27 | -26.71	-6.28 | -20.28	-6.79 | -28.18	-6.22 | -20.34
NICS(f) | NICS(f)$_{zz}$	-2.00 | -8.94	-1.80 | -8.23	-1.61 | -7.92	-3.18 | -11.58	-1.15 | -6.87
NICS(g) | NICS(g)$_{zz}$	-6.14 | -19.79	-6.31 | -20.22	-6.22 | -26.64	-6.75 | -21.41	-6.17 | -26.86

	POPa	POPb	POPc	POPd	POPe
ΔE	0.00	8.16	7.51	24.67	4.36
ΔG_{298}	0.00	8.13	7.65	24.88	4.79
NICS(0) | NICS(1)$_{zz}$	−13.37 | −33.86	−13.05 | −32.46	−13.48 | −33.53	−2.74 | −4.72	−13.07 | −32.05
NICS(a) | NICS(a)$_{zz}$	+8.32 | + 7.67	+8.68 | + 8.77	+8.38 | + 6.65	−7.30 | −23.42	+3.01 | −2.80
NICS(b) | NICS(b)$_{zz}$	−11.48 | −26.31	−2.16 | −11.19	−12.58 | −36.63	+0.45 | −4.91	−2.16 | −16.02
NICS(c) | NICS(c)$_{zz}$	+1.51 | −2.76	−7.89 | −19.45	−8.41 | −20.83	−1.64 | −4.08	−9.51 | −24.10
NICS(d) | NICS(d)$_{zz}$	−12.56 | −36.58	−13.40 | −37.96	−3.12 | −12.92	+0.02 | −8.27	−2.77 | −11.22
NICS(e) | NICS(e)$_{zz}$	−6.19 | −26.73	−6.27 | −26.71	−6.28 | −20.28	−6.79 | −28.18	−6.22 | −20.34
NICS(f) | NICS(f)$_{zz}$	−2.00 | −8.94	−1.80 | −8.23	−1.61 | −7.92	−3.18 | −11.58	−1.15 | −6.87
NICS(g) | NICS(g)$_{zz}$	−6.14 | −19.79	−6.31 | −20.22	−6.22 | −26.64	−6.75 | −21.41	−6.17 | −26.86

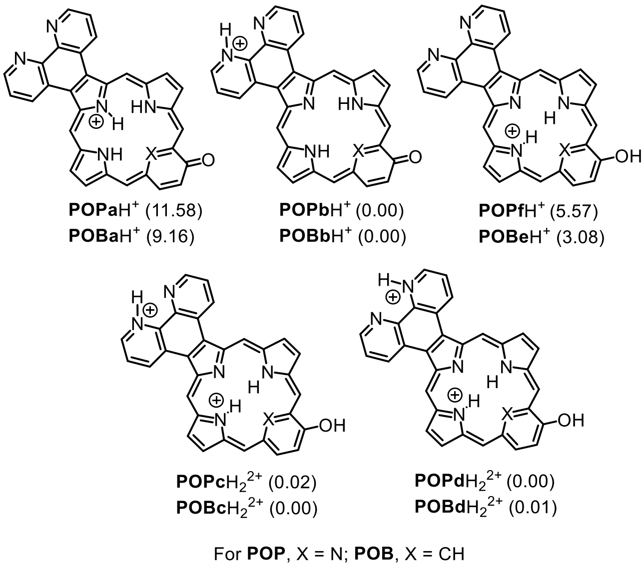

POPaH$^+$ (11.58)
POBaH$^+$ (9.16)

POPbH$^+$ (0.00)
POBbH$^+$ (0.00)

POPfH$^+$ (5.57)
POBeH$^+$ (3.08)

POPcH$_2^{2+}$ (0.02)
POBcH$_2^{2+}$ (0.00)

POPdH$_2^{2+}$ (0.00)
POBdH$_2^{2+}$ (0.01)

For **POP**, X = N; **POB**, X = CH

Figure 19. Selected mono- and diprotonated phenanthrolino-oxypyriporphyrins (POPs) and phenanthrolino-oxybenziporphyrins (POBs). Relative energies (ΔE) in kcal/mol are given in parentheses.

identified. In most cases, NICS(0) and NICS(1)$_{zz}$ calculations demonstrated that these systems retain strongly aromatic properties but AICD plots show that the macrocyclic ring currents can extend around the periphery of the fused phenanthroline units. The computational results were particularly useful in determining the preferred sites for mono- and diprotonation. With the notable exception of a phenanthroline-fused oxaporphyrin, initial protonation was favored on the external phenanthroline unit rather than within the porphyrinoid core. However, the results do not fully explain the observed proton NMR chemical shifts for the free base structures and further studies will be required to resolve these important issues. It is possible that intermolecular interactions are responsible for these observations, but it is not clear why these would consistently manifest for tropone and phenanthroline-fused porphyrinoid structures but never for structurally analogous phenanthroporphyrinoids.

■ EXPERIMENTAL SECTION

Melting points are uncorrected. NMR spectra were recorded using a 400 or 500 MHz NMR spectrometer and were run at 302 K unless otherwise indicated. ^{1}H NMR values are reported as chemical shifts δ, relative integral, multiplicity (s, singlet; d, doublet; dd, doublet of doublets, t, triplet; q, quartet; m, multiplet; br, broad peak), and coupling constant (J). Chemical shifts are reported in parts per million (ppm) relative to $CDCl_3$ (^{1}H residual $CHCl_3$ singlet δ 7.26 ppm, ^{13}C $CDCl_3$ triplet δ 77.23 ppm), and coupling constants were taken directly from the spectra. NMR assignments were made with the aid of ^{1}H−^{1}H COSY, HSQC, DEPT-135, and NOE difference proton NMR spectroscopy. 2D-NMR experiments were performed using standard software. Mass spectral data were acquired using positive-mode electrospray ionization (ESI+) and a high-resolution time-of-flight mass spectrometer.

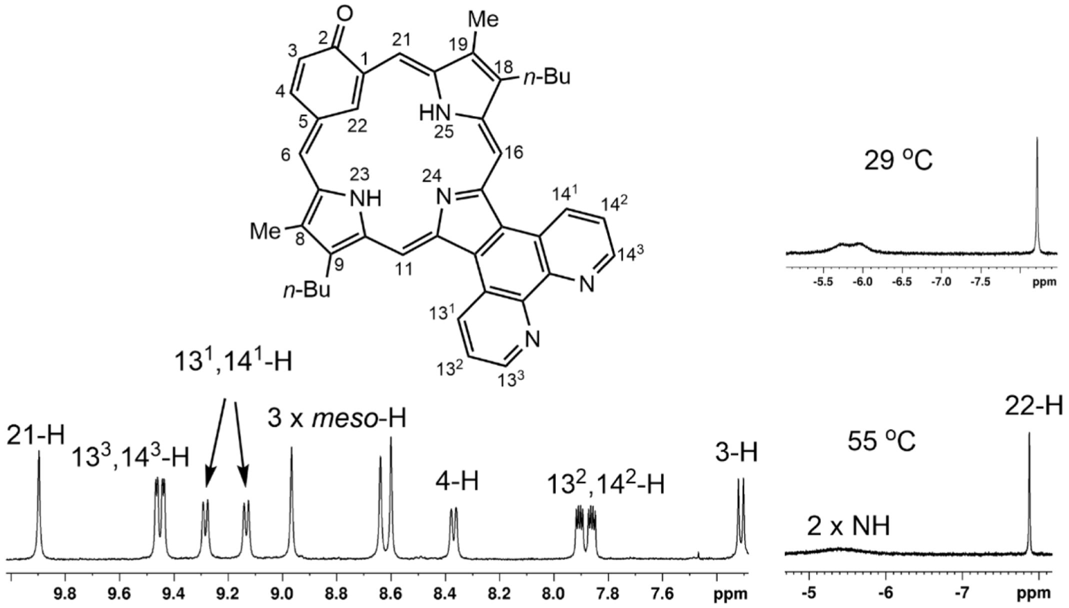

Figure 20. Partial proton NMR spectrum of oxybenziporphyrin **28** in $CDCl_3$ at 55 °C showing details of the upfield and downfield regions.

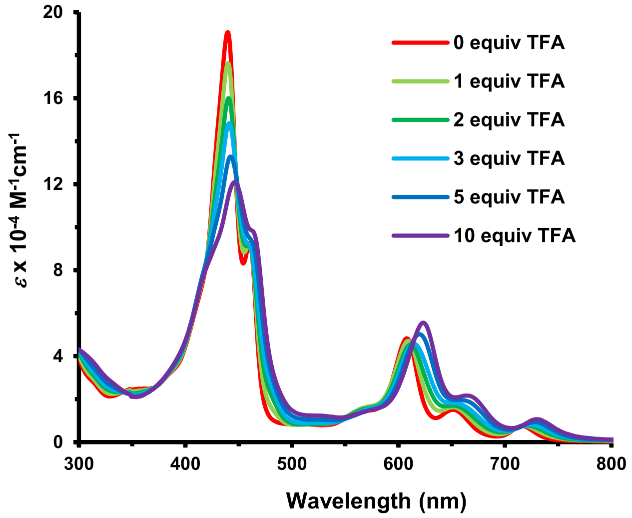

Figure 21. UV–vis spectra of oxybenziporphyrin **28** in CH_2Cl_2 with 0–10 equiv of TFA.

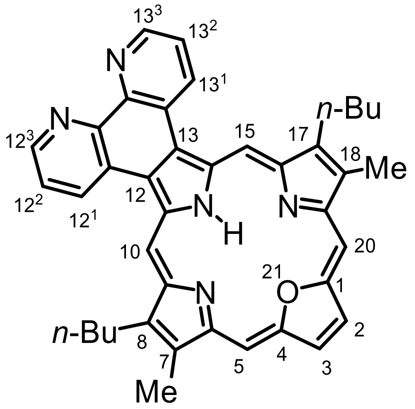

8,17-Dibutyl-7,18-dimethyl-21-oxaphenanthrolino[5,6-*l*]-porphyrin (17). Tripyrrane **13b**[18] (100 mg, 0.139 mmol) was stirred with trifluoroacetic acid (1 mL) under nitrogen for 10 min in a pear-shaped flask. The mixture was diluted with dichloromethane (19 mL), furan dialdehyde **20a** (17 mg, 0.139 mmol) was immediately added, and the mixture stirred for 3 h under nitrogen. The resulting solution was neutralized with triethylamine, DDQ (31 mg, 0.137 mmol) was

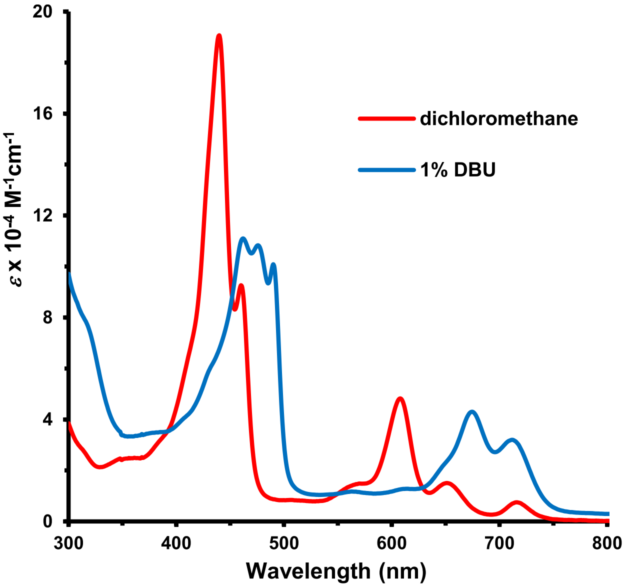

Figure 22. UV–vis spectra of oxybenziporphyrin **28** in CH_2Cl_2 (red line) and 1% DBU-CH_2Cl_2 (blue line).

Scheme 6. Deprotonation of Oxybenziporphyrin 28

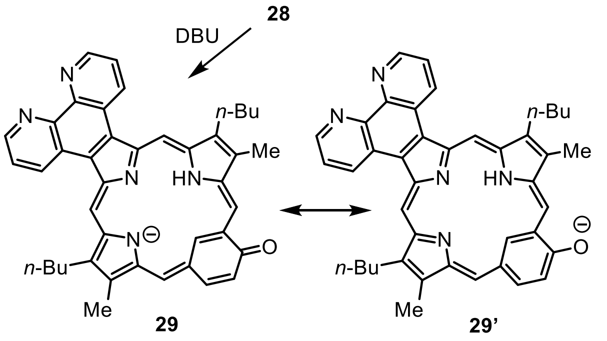

Table 11. Calculated Relative Energies (kcal/mol) and NICS Values for Selected Phenanthrolino-Oxybenziporphyrin Tautomers

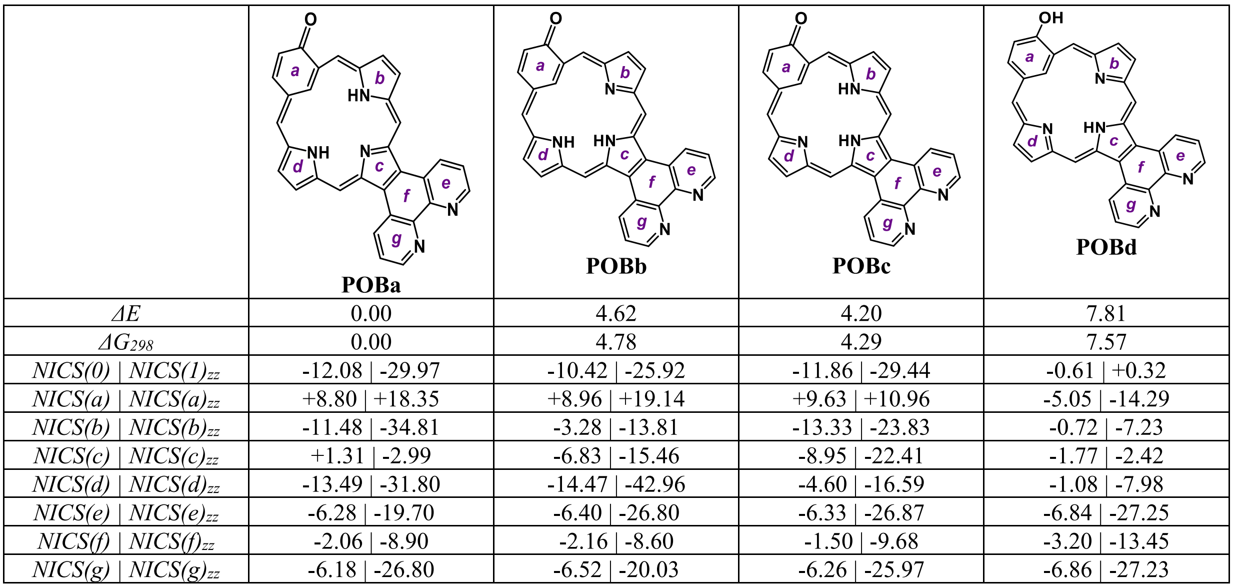

	POBa	POBb	POBc	POBd
ΔE	0.00	4.62	4.20	7.81
ΔG₂₉₈	0.00	4.78	4.29	7.57
NICS(0) | NICS(1)zz	-12.08 | -29.97	-10.42 | -25.92	-11.86 | -29.44	-0.61 | +0.32
NICS(a) | NICS(a)zz	+8.80 | +18.35	+8.96 | +19.14	+9.63 | +10.96	-5.05 | -14.29
NICS(b) | NICS(b)zz	-11.48 | -34.81	-3.28 | -13.81	-13.33 | -23.83	-0.72 | -7.23
NICS(c) | NICS(c)zz	+1.31 | -2.99	-6.83 | -15.46	-8.95 | -22.41	-1.77 | -2.42
NICS(d) | NICS(d)zz	-13.49 | -31.80	-14.47 | -42.96	-4.60 | -16.59	-1.08 | -7.98
NICS(e) | NICS(e)zz	-6.28 | -19.70	-6.40 | -26.80	-6.33 | -26.87	-6.84 | -27.25
NICS(f) | NICS(f)zz	-2.06 | -8.90	-2.16 | -8.60	-1.50 | -9.68	-3.20 | -13.45
NICS(g) | NICS(g)zz	-6.18 | -26.80	-6.52 | -20.03	-6.26 | -25.97	-6.86 | -27.23

	POBa	POBb	POBc	POBd
ΔE	0.00	4.62	4.20	7.81
ΔG_{298}	0.00	4.78	4.29	7.57
NICS(0) | NICS(1)$_{zz}$	−12.08 | −29.97	−10.42 | −25.92	−11.86 | −29.44	−0.61 | + 0.32
NICS(a) | NICS(a)$_{zz}$	+8.80 | + 18.35	+8.96 | + 19.14	+9.63 | + 10.96	−5.05 | −14.29
NICS(b) | NICS(b)$_{zz}$	−11.48 | −34.81	−3.28 | −13.81	−13.33 | −23.83	−0.72 | −7.23
NICS(c) | NICS(c)$_{zz}$	+1.31 | −2.99	−6.83 | −15.46	−8.95 | −22.41	−1.77 | −2.42
NICS(d) | NICS(d)$_{zz}$	−13.49 | −31.80	−14.47 | −42.96	−4.60 | −16.59	−1.08 | −7.98
NICS(e) | NICS(e)$_{zz}$	−6.28 | −19.70	−6.40 | −26.80	−6.33 | −26.87	−6.84 | −27.25
NICS(f) | NICS(f)$_{zz}$	−2.06 | −8.90	−2.16 | −8.60	−1.50 | −9.68	−3.20 | −13.45
NICS(g) | NICS(g)$_{zz}$	−6.18 | −26.80	−6.52 | −20.03	−6.26 | −25.97	−6.86 | −27.23

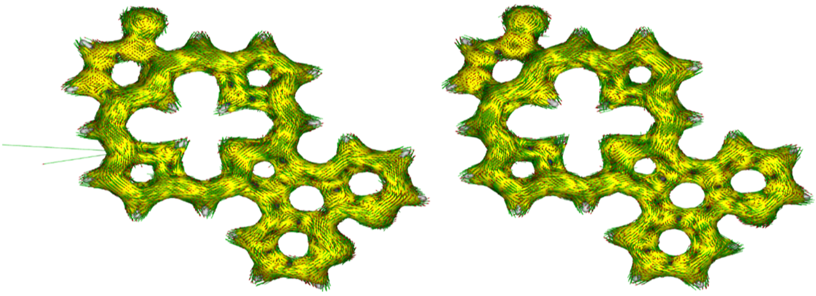

Figure 23. AICD plots (isovalues 0.05) of phenanthroline-fused oxybenziporphyrin **POBa** (left) and monocation **POBbH**$^+$ (right).

added, and stirring was continued for an additional 1 h. The solution was diluted with chloroform and washed with water. The solvent was removed under reduced pressure and the residue was chromatographed on a grade 3 alumina column eluting with 2% methanol-chloroform. A deep green band was collected, and the solvent evaporated under reduced pressure. The residue was recrystallized from chloroform-hexanes to give the oxaporphyrin (37 mg, 0.061 mmol, 44%) as dark green crystals, mp > 300 °C, dec UV−vis (1% $Et_3N-CH_2Cl_2$) λ_{max}/nm (log ε): 375 (sh, 4.67), 393 (sh, 4.74), 418 (4.84), 507 (4.17), 531 (3.79), 561 (3.65), 604 (3.67), 666 (3.91). UV−vis (2 equiv TFA-CH_2Cl_2) λ_{max}/nm (log ε): 365 (sh, 4.48), 409 (5.13), 552 (4.02), 569 (4.02), 593 (4.23). UV−vis (10% TFA-CH_2Cl_2) λ_{max}/nm (log ε): 358 (sh, 4.50), 413 (5.06), 553 (4.05), 569 (4.06), 600 (4.35).

^{1}H NMR (500 MHz, TFA-$CDCl_3$): δ 11.59 (2H, s, 10,15-H), 11.08 (s, 2H, 5,20-H), 10.79 (d, 2H, J = 8.5 Hz, 12^1,13^1-H), 10.58 (s, 2H, 2,3-H), 9.66 (dd, 2H, J = 1.0, 4.6 Hz, 12^3,13^3-H), 8.71 (dd, 2H, J = 4.6, 8.5 Hz, 12^2,13^2-CH), 4.45 (t, 4H, J = 7.8 Hz, 8,17-CH_2), 3.93 (s, 6H, 7,18-Me), 2.46 (p, 4H, J = 7.6 Hz, 8,17-CH_2CH_2), 1.90 (sextet, 4H, J = 7.4 Hz, 2 × CH_2CH_3), 1.24 (t, 6H, J = 7.4 Hz, 2 × CH_2CH_3), −5.09 (br s, 1H, NH).

^{13}C{^{1}H} NMR (125 MHz, TFA-$CDCl_3$): δ 154.2, 150.6, 147.2 (12^3, 13^3-CH), 145.1, 140.1, 139.4, 139.0, 138.8 (12^1, 13^1-CH), 138.3, 136.4, 132.1, 127.2 (12^2, 13^2-CH), 126.8, 105.1 (5,20-CH), 97.7 (10,15-CH), 35.2 (8,17-CH_2CH_2), 26.6 (8,17-CH_2), 23.2 (2 × CH_2CH_3), 14.0 (2 × CH_2CH_3), 11.9 (7,18-Me). HRMS (ESI) m/z: $[M + H]^+$ calcd for $C_{40}H_{38}N_5O$ 604.3071; found, 604.3058.

In order to demonstrate the scalability of this chemistry, the reaction was repeated with 600 mg of tripyrrane **13b** (0.834 mmol), dialdehyde **20a** (102 mg, 0.834 mmol), trifluoroacetic acid (5 mL), dichloromethane (115 mL) and DDQ (186 mg, 0.82 mmol). Recrystallization from chloroform-hexanes gave oxaporphyrin **17** (438.1 mg, 0.726 mmol, 87%) as dark greenish-brown crystals, mp > 300 °C, dec.

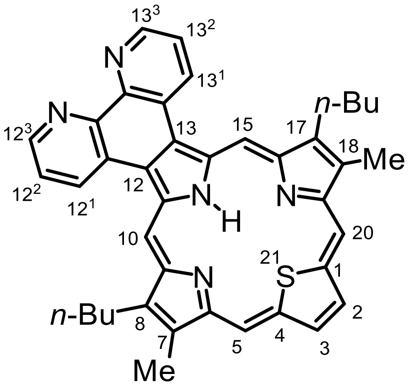

8,17-Dibutyl-7,18-dimethyl-21-thiaphenanthrolino[5,6-*l*]-porphyrin (18). Tripyrrane **13b**[18] (100 mg, 0.139 mmol) was stirred with trifluoroacetic acid (1 mL) under nitrogen for 10 min in a pear-shaped flask. The mixture was diluted with dichloromethane (19 mL), thiophene dialdehyde **20b** (19.5 mg, 0.139 mmol) was immediately added, and the mixture stirred for 3 h under nitrogen. The resulting solution was neutralized with triethylamine. DDQ (31 mg, 0.137 mmol) was added, and stirring was continued for 1 h. The solution was diluted with chloroform and washed with water. The solvent was removed under reduced pressure and the residue was purified on a grade 3 alumina column eluting with 1% methanol-chloroform. A dark red-brown band was collected, and the solvent removed on a rotary evaporator. The residue was recrystallized from chloroform−methanol to give the thiaporphyrin (68 mg, 0.109 mmol, 79%) as reddish-brown crystals, mp > 260 °C, dec UV−vis (CH_2Cl_2) λ_{max}/nm (log ε): 424 (5.07), 512 (4.35), 538 (3.83), 610 (3.44), 619 (3.44), 643 (2.81), 672 (4.08). UV−vis (20 equiv TFA-CH_2Cl_2) λ_{max}/nm (log ε): 425 (5.24), 571 (4.07), 582 (sh, 4.06), 613 (4.14). UV−vis (1% TFA-CH_2Cl_2) λ_{max}/nm (log ε): 431 (5.17), 573 (4.10), 618 (4.26). ^{1}H NMR (500 MHz, $CDCl_3$): δ 10.42 (2H, s, 5,20-H), 9.96 (s, 2H, 2,3-H), 9.80 (br s, 2H, 10,15-H), 9.40 (d, 2H, J = 3.8 Hz, 12^3,13^3-H), 9.33 (br, 2H, 12^1,13^1-H), 7.74−7.72 (m, 2H, 12^2,13^2-CH), 3.35 (br t, 4H, 8,17-CH_2), 3.25 (s, 6H, 7,18-Me), 2.00 (p, 4H, J = 7.4 Hz, 8,17-CH_2CH_2), 1.66 (sextet, 4H, J = 7.3 Hz, 2 × CH_2CH_3), 1.07 (t, 6H, J = 7.4 Hz, 2 × CH_2CH_3), −4.49 (br s, 1H, NH). ^{13}C{^{1}H} NMR (125 MHz, TFA-$CDCl_3$): δ 157.2, 153.7, 149.6 (12^3,13^3-CH), 148.0, 146.8, 144.8, 138.6, 133.8 (2,3-CH), 133.2 (12^1,13^1-CH), 132.1, 127.2, 125.2, 123.5 (12^2,13^2-CH), 113.3 (5,20-CH), 100.2 (10,15-CH), 35.4 (8,17-CH_2CH_2), 26.2 (8,17-CH_2), 23.4 (2 × CH_2CH_3), 14.3 (2 × CH_2CH_3), 11.5 (7,18-Me). ^{1}H NMR (500 MHz, TFA-$CDCl_3$): δ 11.61 (2H, s, 10,15-H), 11.49 (s, 2H, 5,20-H), 10.77 (dd, 2H, J = 1.2, 8.6 Hz, 12^1,13^1-H), 10.53 (s, 2H, 2,3-H), 9.61 (dd, 2H, J = 1.2, 4.8 Hz, 12^3,13^3-H), 8.71 (dd, 2H, J = 4.6, 8.5 Hz, 12^2,13^2-CH), 4.38 (t, 4H, J = 7.8 Hz, 8,17-CH_2), 3.88 (s, 6H, 7,18-Me), 2.43 (p, 4H, J = 7.6 Hz, 8,17-CH_2CH_2), 1.89 (sextet, 4H, J = 7.4 Hz, 2 × CH_2CH_3), 1.22 (t, 6H, J = 7.4 Hz, 2 × CH_2CH_3). ^{13}C{^{1}H} NMR (125 MHz, TFA-$CDCl_3$): δ 152.1, 147.3 (12^3,13^3-CH), 147.2, 145.0, 142.0, 141.7, 141.0, 139.5 (12^1,13^1-CH), 139.3, 136.6, 127.5 (12^2,13^2-CH), 126.9, 111.9 (5,20-CH), 105.4 (10,15-CH), 35.3 (8,17-CH_2CH_2), 26.6 (8,17-CH_2), 23.6 (2 × CH_2CH_3), 14.1 (2 × CH_2CH_3), 12.2 (7,18-Me). HRMS (ESI) m/z: $[M + H]^+$ calcd for $C_{40}H_{38}N_5S$ 620.2842; found, 620.2843.

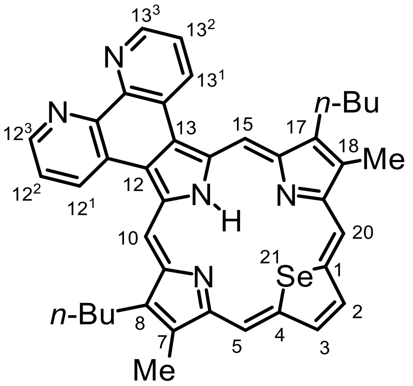

8,17-Dibutyl-7,18-dimethyl-21-selenaphenanthrolino[5,6-*l*]porphyrin (19). Tripyrrane **13b**[18] (100 mg, 0.139 mmol) was stirred with trifluoroacetic acid (1 mL) under nitrogen for 10 min in a pear-shaped flask. The mixture was diluted with dichloromethane (19 mL), selenophene dialdehyde **20c** (26.0 mg, 0.139 mmol) was immediately added, and the mixture stirred for 3 h under nitrogen. The resulting solution was neutralized with triethylamine. DDQ (31 mg, 0.137 mmol) was added, and stirring was continued for an additional 1 h. The solution was diluted with chloroform and washed with water. The solvent was removed under reduced pressure and the residue was chromatographed on a grade 3 alumina column eluting with 1% methanol-chloroform. A dark red-brown band was collected, and the solvent removed under reduced pressure. The residue was recrystallized from chloroform−methanol to give the selenaporphyrin (51.1 mg, 0.0766 mmol, 55%) as dark red-brown crystals, mp > 260 °C, dec UV−vis (CH_2Cl_2) λ_{max}/nm (log ε): 399 (5.03), 421 (5.38), 520 (4.07), 559 (4.66), 579 (4.38), 633 (3.46), 644 (sh, 3.41). UV−vis (100 equiv TFA-CH_2Cl_2) λ_{max}/nm (log ε): 384 (sh, 4.65), 434 (4.93), 523 (4.25), 584 (3.58), 630 (3.64), 688 (4.21). ^{1}H NMR (500 MHz, $CDCl_3$): δ 10.55 (s, 2H, 5,20-H), 10.24 (s, 2H, 2,3-H), 9.78 (br s, 2H, 10,15-H), 9.42 (br d, 2H, J = 4.0 Hz, 12^3,13^3-H), 9.32−9.28 (br m, 2H, 12^1,13^1-H), 7.73 (dd, 2H, J = 3.7, 7.7 Hz, 12^2,13^2-H), 3.27 (t, 4H, J = 7.4 Hz, 8,17-CH_2), 3.22 (s, 6H, 7,18-Me), 1.98 (p, 4H, J = 7.4 Hz, 8,17-CH_2CH_2), 1.66 (sextet, 4H, J = 7.3 Hz, 2 × $CH_2CH_2CH_3$), 1.07 (t, 6H, J = 7.4 Hz, 2 × $CH_2CH_2CH_3$), −4.81 (br s, 1H). ^{1}H NMR (500 MHz, $CDCl_3$, 55 °C): δ 10.60 (s, 2H, 5,20-H), 10.26 (s, 2H, 2,3-H), 10.08 (s, 2H, 10,15-H), 9.55 (d, 2H, J = 8.2 Hz, 12^1,13^1-H), 9.48 (dd, 2H, J = 1.1, 4.0 Hz, 12^3,13^3-H), 7.81 (dd, 2H, J = 4.0, 8.2 Hz, 12^2,13^2-H), 3.43 (t, 4H, J = 7.9 Hz, 8,17-CH_2), 3.27 (s, 6H, 7,18-Me), 2.08 (p, 4H, J = 7.7 Hz, 8,17-CH_2CH_2), 1.72 (sextet, 4H, J = 7.3 Hz, 2 × $CH_2CH_2CH_3$), 1.12 (t, 6H, J = 7.4 Hz, 2 × $CH_2CH_2CH_3$), −4.38 (br s, 1H). ^{1}H NMR (500 MHz, TFA-$CDCl_3$): δ 11.53 (s, 2H), 11.50 (s, 2H) (4 × *meso*-H), 10.73 (dd, 2H, J = 1.0, 8.6 Hz, 12^1,13^1-H), 10.31 (s, 2H, 2,3-H), 9.58 (dd, 2H, J = 0.9, 4.8 Hz, 12^3,13^3-H), 8.69 (dd, 2H, J = 4.8, 8.5 Hz, 12^2,13^2-H), 4.31 (t, 4H, J = 7.8 Hz), 3.81 (s, 6H), 2.38 (p, 4H, J = 7.6 Hz), 1.86 (sextet, 4H, J = 7.4 Hz), 1.20 (t, 6H, J = 7.4 Hz). ^{13}C{^{1}H} NMR (125 MHz TFA-$CDCl_3$): δ 149.0 (br), 147.3 (12^3,13^3-CH), 146.5, 145.9 (br), 142.5, 140.9, 139.7 (12^1,13^1-CH), 139.4, 138.6 (2,3-CH), 135.4 (br), 127.6 (12^2,13^2-CH), 126.9, 117.4 (10,15-CH), 105.0 (5,20-CH), 35.2 (8,17-CH_2CH_2), 26.6 (8,17-CH_2), 23.4 (2 × $CH_2CH_2CH_3$), 14.1 (2 × $CH_2CH_2CH_3$), 12.0 (7,18-Me), HRMS (ESI) m/z: $[M + H]^+$ calcd for $C_{40}H_{38}N_5Se$ 668.2287; found 668.2281.

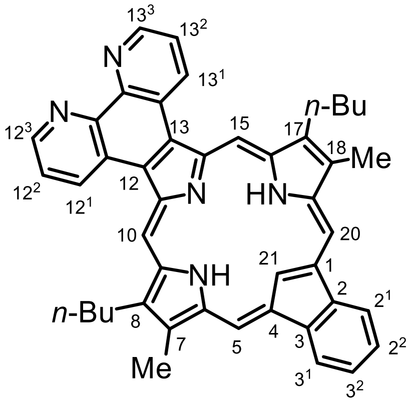

8,17-Dibutyl-7,18-dimethylbenzo[*b*]phenanthrolino[5,6-*l*]-21-carbaporphyrin (23). Tripyrrane **13b**[18] (100 mg, 0.139 mmol) was stirred with trifluoroacetic acid (1 mL) under nitrogen for 10 min in a pear-shaped flask. The mixture was diluted with dichloromethane (19 mL), indene dialdehyde **22**[31] (23.9 mg, 0.139 mmol) was immediately added, and the mixture stirred for 3 h under nitrogen. The flask was covered in aluminum foil to protect the reactants from light. The resulting solution was neutralized with triethylamine. DDQ (31 mg, 0.137 mmol) was added, and stirring was continued for an additional 1 h. The solution was diluted with chloroform and washed with water. The solvent was removed under reduced pressure and the residue was chromatographed on a grade 3 alumina column eluting with 1%

methanol-chloroform. A green band was collected, and the solvent was removed. The residue was recrystallized from chloroform−methanol to give the carbaporphyrin (42.7 mg, 0.070 mmol, 47%) as dark purple crystals, mp > 260 °C. UV−vis (CH_2Cl_2) λ_{max}/nm (log ε): 389 (4.51), 444 (5.23), 500 (3.95), 536 (3.95), 575 (4.46), 620 (3.91). UV−vis (100 equiv TFA-CH_2Cl_2) λ_{max}/nm (log ε): 400 (4.56), 453 (4.89), 603 (4.36), 644 (sh, 4.11), 704 (sh, 3.52). UV−vis (3000 equiv TFA-CH_2Cl_2) λ_{max}/nm (log ε): 398 (sh, 4.50), 474 (4.92), 584 (3.91), 638 (4.31), 722 (sh, 3.62). UV−vis (1% TFA-CH_2Cl_2) λ_{max}/nm (log ε): 398 (sh, 4.50), 472 (4.91), 499 (sh, 4.74), 585 sh, (3.88), 637 (4.18), 723 (sh, 3.58). UV−vis (50% TFA-CH_2Cl_2) λ_{max}/nm (log ε): 399 (4.56), 451 (4.89), 601 (4.35), 644 (sh, 4.07). ^{1}H NMR (500 MHz, $CDCl_3$, 55 °C): δ 9.37 (2H, d, J = 3.6 Hz, 12^3,13^3-H), 9.05 (s, 2H, 10,15-H), 9.01 (d, 2H, J = 7.7 Hz, 12^1,13^1-H), 8.63 (s, 2H, 5,20-H), 8.47−8.45 (m, 2H, 2^1,3^1-H), 7.72−7.69 (m, 4H, 2^2,3^2-H and 12^2,13^2-H), 3.03 (t, 4H, J = 7.8 Hz, 8,17-CH_2), 2.87 (s, 6H, 7,18-Me), 1.70 (p, 4H, J = 7.6 Hz, 8,17-CH_2CH_2), 1.48 (sextet, 4H, J = 7.3 Hz, 2 × CH_2CH_3), 1.00 (t, 6H, J = 7.3 Hz, 2 × CH_2CH_3), −6.83 (br s, 2H, 2 × NH), −8.84 (s, 1H, 21-H). ^{13}C{^{1}H} NMR (125 MHz, $CDCl_3$, 55 °C): δ 148.9 (12^3,13^3-CH), 146.8, 141.4, 136.3, 135.4, 134.4, 134.0, 132.8 (12^1,13^1-CH), 132.0, 127.0 (2^1,3^1-CH), 125.4, 123.2 (12^2,13^2-CH), 120.7 (2^1,3^1-CH), 109.5, 98.2 (5,20-CH), 96.8 (10,15-CH), 34.8 (8,17-CH_2CH_2), 25.6 (8,17-CH_2), 23.3 (2 × $CH_2CH_2CH_3$), 14.1 (2 × CH_2CH_3), 11.0 (7,18-Me). ^{1}H NMR (500 MHz, TFA-$CDCl_3$): δ 10.75 (s, 2H, 10,15-H), 10.65 (d, 2H, J = 8.4 Hz, 12^1,13^1-H), 10.25 (s, 2H, 5,20-H), 9.56 (d, 2H, J = 4.7 Hz, 12^3,13^3-H), 8.63 (dd, 2H, J = 4.8, 8.4 Hz, 12^2,13^2-H), 8.59−8.55 (m, 2H, 2^1,3^1-H), 7.71−7.67 (m, 2H, 2^2,3^2-H), 4.08 (t, 4H, J = 7.7 Hz, 8,17-CH_2), 3.56 (s, 6H, 7,18-Me), 2.06 (p, 4H, J = 7.5 Hz, 8,17-CH_2CH_2), 1.66 (sextet, 4H, J = 7.4 Hz, 2 × CH_2CH_3), 1.07 (t, 6H, J = 7.4 Hz, 2 × CH_2CH_3), −1.58 (br s, 2H, 2 × NH), −6.14 (s, 1H, 21-H). ^{13}C{^{1}H} NMR (125 MHz, TFA-$CDCl_3$): δ 146.9 (12^3,13^3-CH), 144.4, 141.8, 141.2, 140.8, 139.5, 139.2 (12^1,13^1-CH), 139.0, 136.8, 131.0, 129.2 (2^2,3^2-CH), 127.8, 127.3 (12^2,13^2-CH), 124.8, 122.4 (21-CH), 122.2 (2^1,3^1-CH), 105.6 (5,20-CH), 95.5 (10,15-CH), 34.6 (8,17-CH_2CH_2), 26.7 (8,17-CH_2), 23.3 (2 × CH_2CH_3), 14.1 (2 × CH_2CH_3), 12.1 (7,18-Me). HRMS (ESI) m/z: $[M + H]^+$ calcd for $C_{45}H_{42}N_5$ 652.3435; found, 652.3438.

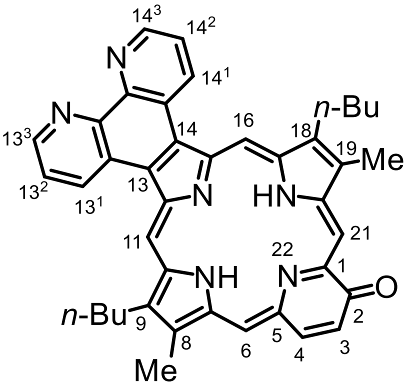

9,18-Dibutyl-8,19-dimethylphenanthrolino[5,6-*m*]-2-oxypyriporphyrin (26). Tripyrrane **13b**[18] (100 mg, 0.139 mmol) was stirred with trifluoroacetic acid (1 mL) under nitrogen for 10 min in a pear-shaped flask. The mixture was diluted with dichloromethane (19 mL), dialdehyde **25a** (21 mg, 0.139 mmol) was immediately added, and the mixture stirred for 3 h under nitrogen. The resulting solution was neutralized with triethylamine. DDQ (31 mg, 0.137 mmol) was added, and stirring was continued for an additional 1 h. The solution was diluted with chloroform and washed with water. The solvent was removed under reduced pressure and the residue was chromatographed on a grade 3 alumina column eluting with 1% methanol-chloroform. A deep green band was collected, and the solvent was removed under reduced pressure. The residue was recrystallized from chloroform−methanol to give the oxypyriporphyrin (51 mg, 0.081 mmol, 58%) as dark green crystals, mp > 285 °C. UV−vis (CH_2Cl_2) λ_{max}/nm (log ε): 348 (4.11), 432 (5.28), 601 (4.48), 627 (4.62), 673 (2.83). UV−vis (300 equiv TFA-CH_2Cl_2) λ_{max}/nm (log ε): 436 (5.01), 611 (sh, 4.38), 642 (4.64), 682 (3.60). UV−vis (1% TFA-CH_2Cl_2) λ_{max}/nm (log ε): 413 (sh, 4.90), 434 (5.12), 558 (3.68), 606 (4.52), 668 (4.08), 733 (4.22). UV−vis (10% TFA-CH_2Cl_2) λ_{max}/nm (log ε): 448 (5.30), 582 (3.86), 615 (3.90), 675 (4.49), 740 (3.03). ^{1}H NMR (500 MHz, $CDCl_3$): δ 10.30 (s, 1H, 21-H), 9.40 (d, 1H, J = 3.4 Hz), 9.39 (d, 1H, J = 3.4 Hz) (13^3,14^3-H), 8.99 (br d, 1H, J = 7.6 Hz), 8.89 (d, 1H, J = 9.1 Hz, 4-H), 8.82 (1H, s), 8.78−8.73 (overlapping d and s), 8.49 (br s, 1H), 7.79 (d, 1H, J = 9.1 Hz, 3-H), 7.76 (dd, 1H, J = 3.6, 7.7 Hz), 7.70 (dd, 1H, J = 4.0, 7.8 Hz) (13^2,14^2-H), 3.09 (t, 2H, J = 7.8 Hz), 3.06 (s, 3H), 3.02 (s, 3H), 2.78 (br t, 2H, J = 7.8 Hz), 1.74−1.67 (m, 2H), 1.52−1.42 (m, 4H), 1.31 (sextet, 2H, J = 7.2 Hz), 0.97 (t, 3H, J = 7.4 Hz), 0.86 (t, 3H, J = 7.3 Hz), −5.97 (br s, 2H), −6.11 (br s, 1H) (2 × NH). ^{13}C{^{1}H} NMR (125 MHz $CDCl_3$): δ 184.9 (C═O), 149.44, 149.42, 148.4, 148.0, 146.2, 146.1, 145.4, 144.5, 138.5, 138.1, 137.7, 136.8, 136.5, 136.3, 135.5, 134.9, 133.7, 133.37, 133.30, 132.09, 132.06, 131.6, 124.70, 124.65, 123.6, 123.5, 107.8, 103.0, 98.0, 97.3, 34.7, 34.4, 25.5, 25.2, 23.1, 23.0, 14.0, 13.9, 11.4, 11.3. ^{1}H NMR (500 MHz, TFA-$CDCl_3$): δ 11.00 (s, 1H), 10.99 (s, 1H), 10.89 (s, 1H), 10.46 (dd, 2H, J = 1.2, 8.5 Hz), 10.02 (s, 1H), 9.71 (d, 1H, J = 9.7 Hz), 9.61 (br d, 2H, J = 4.9 Hz), 8.71 (dd, 2H, J = 4.9, 8.5 Hz), 8.59 (d, 1H, J = 9.6 Hz), 4.01 (t, 4H, J = 7.7 Hz), 3.49 (s, 3H), 3.46 (s, 3H), 1.98−1.91 (m, 4H), 1.57−1.48 (m, 4H), 0.98−0.95 (2 overlapping triplets, 6H). ^{13}C{^{1}H} NMR (125 MHz TFA-$CDCl_3$): δ 179.0 (C═O), 148.4, 148.1, 146.5, 145.5, 145.2, 145.1, 144.9, 144.8, 143.1, 141.3, 140.4, 140.0, 139.80, 139.78, 139.2, 137.1, 135.1, 134.7, 128.17, 128.11, 127.7, 127.4, 126.5, 106.9, 102.9, 102.4, 102.2, 34.3, 26.6, 23.0, 13.7, 12.2, 12.0. HRMS (ESI) m/z: $[M + H]^+$ calcd for $C_{41}H_{39}N_6O$ 631.3180; found, 631.3181.

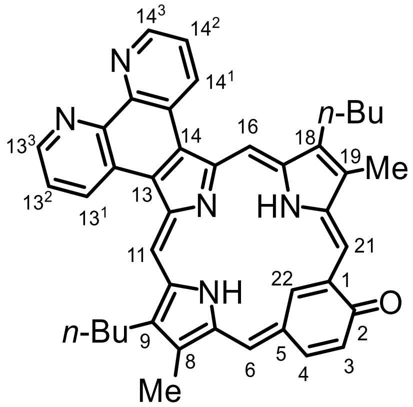

9,18-Dibutyl-8,19-dimethylphenanthrolino[5,6-*m*]-2-oxybenziporphyrin (28). Tripyrrane **13b**[18] (100 mg, 0.139 mmol) was stirred with trifluoroacetic acid (1 mL) under nitrogen for 10 min in a pear-shaped flask. The mixture was diluted with dichloromethane (19 mL), dialdehyde **25b** (21 mg, 0.139 mmol) was immediately added, and the mixture stirred for 3 h under nitrogen. The resulting solution was neutralized with triethylamine, DDQ (31 mg, 0.137 mmol) was added, and stirring was continued for a further 1 h. The solution was diluted with chloroform and washed with water. The solvent was removed under reduced pressure and the residue was chromatographed on a grade 3 alumina column eluting with 1% methanol-chloroform. A dark pinkish-red band was collected, and the solvent was removed on a rotary evaporator The residue was recrystallized from chloroform−methanol and oxybenziporphyrin **28** (51 mg, 0.081 mmol, 58%) was isolated as green crystals, mp > 285 °C, dec UV−vis (CH_2Cl_2) λ_{max}/nm (log ε): 440 (5.14), 460 (4.83), 608 (4.54), 651 (4.04), 716 (3.73). UV−vis (20 equiv TFA-CH_2Cl_2) λ_{max}/nm (log ε): 448 (4.94), 464 (sh, 4.86), 624 (4.61), 666 (4.21), 733 (3.90). UV−vis (1000 equiv TFA-CH_2Cl_2) λ_{max}/nm (log ε): 455 (4.99), 486 (4.75), 647 (4.36), 734 (3.94), 823 (3.39). UV−vis (1% TFA-CH_2Cl_2) λ_{max}/nm (log ε): 377 (sh, 4,43), 449 (5.00), 485 (4.56), 610 (sh, 4.20), 640 (4.33), 736 (3.88), 831 (3.56). UV−vis (10% TFA-CH_2Cl_2) λ_{max}/nm (log ε): 371 (4.62), 444 (4.87), 575 (sh, 3.98), 624 (4.36), 717 (3.82), 787 (3.87). UV−vis (1% DBU-CH_2Cl_2) λ_{max}/nm (log ε): 462 (4.90), 476 (4.89), 490 (4.86), 675 (4.49), 712 (4.36). ^{1}H NMR (500 MHz, $CDCl_3$): δ 9.80 (s, 1H, 21-H), 9.46 (d, 1H, J = 3.2 Hz), 9.43 (d, 1H, J = 3.3 Hz) (13^3,14^3-H), 9.16 (d, 1H, J = 8.0 Hz), 9.00 (d, 1H, J = 8.0 Hz) (13^1,14^1-H), 8.73 (s, 1H), 8.46 (s, 1H), 8.38 (s, 1H) (3 × *meso*-H), 8.31 (d, 1H, J

= 8.9 Hz, 4-H), 7.89 (dd, 1H, *J* = 3.6, 8.0 Hz), 7.85 (dd, 1H, *J* = 3.9, 7.9 Hz) (13^2,14^2-H), 7.29 (d, 1H, *J* = 9.1 Hz, 3-H), 3.19 (t, 2H, *J* = 7.8 Hz), 3.00−2.95 (overlapping t and s, 5H), 2.90 (s, 3H), 1.76−1.46 (m, 6H), 1.39 (sextet, 2H, *J* = 7.2 Hz), 1.01 (t, 3H, *J* = 7.4 Hz), 0.94 (t, 3H, *J* = 7.4 Hz), −5.73 (br s, 1H), −5.95 (s, 1H), −8.22 (s, 1H). ^{1}H NMR (500 MHz, $CDCl_3$ 55 °C): *δ* 9.90 (s, 1H), 9.46 (br d, 1H, *J* = 3.7 Hz), 9.44 (br d, 1H, *J* = 3.7 Hz), 9.28 (d, 1H, *J* = 8.1 Hz), 9.13 (d, 1H, *J* = 8.1 Hz), 8.97 (s, 1H), 8.64 (s, 1H), 8.60 (s, 1H), 8.37 (d, 1H, *J* = 9.2 Hz), 7.90 (dd, 1H, *J* = 3.9, 8.1 Hz), 7.86 (dd, 1H, *J* = 3.9, 8.1 Hz), 7.31 (d, 1H, *J* = 9.2 Hz), 3.32 (t, 2H, *J* = 8.0 Hz), 3.11 (t, 2H, *J* = 8.0 Hz), 3,06 (s, 3H), 3.01 (s, 3H), 1.83 (p, 2H, *J* = 7.6 Hz), 1.69 (p, 2H, *J* = 7.6 Hz), 1.60−1.43 (m, 4H), 1.06 (t, 3H, *J* = 7.4 Hz), 0.99 (t, 3H, *J* = 7.4 Hz), −5.4 (v br, 2H), −7.88 (s, 1H). ^{13}C{^{1}H} NMR (125 MHz, $CDCl_3$, 55 °C): *δ* 187.3, 149.7, 148.4, 147.0, 146.9, 146.5, 138.5, 137.6, 136.8, 136.0, 135.55, 135.47, 134.0, 133.6, 133.3, 132.4, 131.9, 130.5, 126.3, 124.84, 124.81, 123.7, 123.6, 122.2, 112.1, 111.1, 105.6, 97.2, 95.0, 34.6, 34.2, 25.5, 25.2, 23.2, 23.1, 14.1, 14.0, 11.5, 11.4. ^{1}H NMR (500 MHz, $CDCl_3$): *δ* 10.2 (br d, 2H, *J* = 8.4 Hz, 13^1,14^1-H), 9.56 (s, 1H, 21-H), 9.51 (br d, 2H, *J* = 4.9 Hz, 13^3,14^3-H), 9.05 (s, 1H), 9.02 (s, 1H), 8.98 (s, 1H) (3 × *meso*-H, 8.63 (dd, 1H, *J* = 2.0, 8.8 Hz, 4-H), 8.56 (d, 1H, *J* = 8.5 Hz), 8.55 (d, 1H, *J* = 8.5 Hz) (13^2,14^2-H), 7.60 (d, 1H, *J* = 8.8 Hz, 3-H), 6.09 (br s, 1H), 6.02 (br s, 1H) (2 × NH), 3.41−3.37 (2 overlapping triplets, 4H, 9,18-CH_2), 3.02 (s, 3H), 3.01 (s, 3H) (8,19-Me), 1.86−1.80 (m, 4H, 9,18-CH_2CH_2), 1.59−1.50 (m, 4H, 2 × CH_2CH_3), 1.48 (br d, 1H, 22-H), 1.03−0.99 (2 overlapping triplets, 6H, 2 × CH_2CH_3). ^{13}C{^{1}H} NMR (125 MHz, TFA-$CDCl_3$): *δ* 172.0, 156.8, 155.0, 149.5, 149.4, 148.9, 148.8, 148.4, 145.0, 143.7, 143.0, 142.1, 141.2, 139.81, 139.74, 139.4, 131.0, 130.5, 130.1, 128.1, 126.08, 126.05, 125.5, 122.51, 122.49, 121.1, 113.7, 98.2, 96.8, 33.3, 33.2, 25.46, 25.44, 23.0, 13.5, 11.3. HRMS (ESI) *m*/*z*: $[M + H]^+$ calcd for $C_{42}H_{40}N_5O$ 630.3227; found, 630.3247.

Proton NMR Spectra for Reference Compounds. The NMR spectra for **9b**, **21b**, **21c**, **27a** and **27b** were previously obtained in the presence of TFA and/or in alternative solvents.[10,20] In order for comparisons to be made, the following proton NMR spectra for the free base forms in $CDCl_3$ are reported for the first time. In addition, the proton NMR spectrum of phenanthrolinopyrrole **11** was previously reported using DMSO-d_6 as a solvent[18] and the proton NMR spectrum of **11** in $CDCl_3$ is also provided below for reference purposes.

7,18-Dibutyl-12,13-diethyl-8,17-dimethylphenanthrolino-[5,6-*b*]porphyrin (9b).[10] ^{1}H NMR ($CDCl_3$, 500 MHz, 55 °C): *δ* 10.14 (br s, 2H, 5,20-H), 9.89 (s, 2H, 10,15-H), 9.70 (br d, 2H, *J* = 8.0 Hz), 9.40 (br d, 2H, *J* = 3.8 Hz, 12^3,13^3-H), 7.86 (dd, 2H, *J* = 3.9, 8.0 Hz, 12^1,13^1-H), 4.02 (q, 4H, *J* = 7.8 Hz, 12,13-CH_2), 3.68 (br t, 4H, *J* = 7.0 Hz, 7,18-CH_2), 3.52 (s, 6H, 8,17-Me), 2.12 (p, 4H, *J* = 7.6 Hz, 7,18-CH_2CH_2), 1.70 (sextet, 4H, *J* = 7.2 Hz, 2 × $CH_2CH_2CH_3$), 1.11 (t, 6H, *J* = 7.4 Hz, 2 × $CH_2CH_2CH_3$), −4.07 (br s, 2H).

8,17-Diethyl-7,18-dimethyl-21-thiaphenanthro[9,10-*l*]-porphyrin (21b).[20] ^{1}H NMR ($CDCl_3$, 500 MHz, 55 °C): *δ* 11.15 (s, 2H, 10,15-H), 10.67 (s, 2H, 5,20-H), 10.09 (d, 2H, *J* = 8.2 Hz, 12^1,13^1-H), 10.08 (s, 2H, 2,3-H), 9.18 (d, 2H, *J* = 8.2 Hz, 12^4,13^4-H), 8.21−8.18 (m, 2H, 12^2,13^2-H), 8.03−8.00 (m, 2H, 12^3,13^3-H), 4.00 (q, 4H, *J* = 7.7 Hz, 8,17-CH_2), 3.45 (s, 6H, 7,18-Me), 1.95 (t, 6H, *J* = 7.7 Hz, 2 × CH_2CH_3), −3.21 (br s, 1H).

8,17-Diethyl-7,18-dimethyl-21-selenaphenanthro[9,10-*l*]-porphyrin (21c).[20] ^{1}H NMR ($CDCl_3$, 500 MHz, 55 °C): *δ* 11.28 (s, 2H, 10,15-H), 10.87 (s, 2H, 5,20-H), 10.41 (s, 2H, 2,3-H), 10.14 (d, 2H, *J* = 8.3 Hz, 12^1,13^1-H), 9.20 (d, 2H, *J* = 8.1 Hz, 12^4,13^4-H), 8.22 (t, 2H, *J* = 7.7 Hz, 12^2,13^2-H), 8.03 (t, 2H, *J* = 7.5 Hz, 12^3,13^3-H), 4.02 (q, 4H, *J* = 7.7 Hz, 8,17-CH_2), 3.47 (s, 6H, 7,18-Me), 1.97 (t, 6H, *J* = 7.7 Hz, 2 × CH_2CH_3), −3.40 (br s, 1H).

9,18-Diethyl-8,19-dimethylphenanthro[9,10-*m*]-2-oxypyriporphyrin (27a).[10] ^{1}H NMR ($CDCl_3$, 500 MHz, 55 °C): *δ* 10.60 (s, 1H), 10.00 (s, 1H), 9.98 (s, 1H) (3 × *meso*-H), 9.48 (d, 1H, *J* = 7.9 Hz), 9.45 (d, 1H, *J* = 7.9 Hz) (13^1,14^1-H), 9.06 (s, 1H, 6-H), 9.03 (m, 3H, 4-H and 13^4,14^4-H), 8.04−8.01 (m, 2H, 13^2,14^2-H), 7.90 (t, 2H, *J* = 7.4 Hz, 13^3,14^3-H), 7.85 (d, 1H, *J* = 9.2 Hz, 3-H), 3.79−3.73 (m, 4H, 2 × CH_2CH_3), 3.45 (s, 3H), 3.30 (s, 3H) 8,19-Me), 1.70−1.66 (m, 6H, 2 × CH_2CH_3), −4.79 (br s, 2H, 2 × NH).

9,18-Diethyl-8,19-dimethylphenanthro[9,10-*m*]-2-oxybenziporphyrin (27b).[10] ^{1}H NMR ($CDCl_3$, 500 MHz, 55 °C): *δ* 10.13 (s, 1H), 9.74 (s, 1H), 9.65 (s, 1H) (3 × *meso*-H), 9.39−9.35 (m, 2H, 13^1,14^1-H), 8.97 (dd, 2H, *J* = 2.5, 8.2 Hz, 13^4,14^4-H), 8.90 (s, 1H, 6-H), 8.53 (d, 1H, *J* = 1.5, 9.3 Hz, 4-H), 7.98 (t, 2H, *J* = 7.4 Hz, 13^2,14^2-H), 7.86 (*t*, 2H, *J* = 7.4 Hz, 13^3,14^3-H), 7.37 (d, 1H, *J* = 9.3 Hz, 3-H), 3.71−3.63 (m, 4H, 2 × CH_2CH_3), 3.31 (s, 3H), 3.21 (s, 3H) (8,19-Me), 1.65−1.60 (2 overlapping triplets, 6H, 2 × CH_2CH_3), −6.90 (s, 1H).

Phenanthrolino[5,6-*c*]pyrrole 11.[18] ^{1}H NMR ($CDCl_3$, 500 MHz, 55 °C): *δ* 9.04 (v br, 1H), 8.96 (dd, 2H, *J* = 1.6, 4.4 Hz, 6,9-H), 8.33 (dd, 2H, *J* = 1.6, 8.0 Hz, 4,11-H), 7.65 (d, 2H, *J* = 2.8 Hz, 1,3-H), 7.48 (dd, 2H, *J* = 4.4, 8.0 Hz, 5,10-H).

Computational Studies. All calculations were performed using the Gaussian 16 revision C.01.[33] Geometry optimizations were performed using the M06-2X functional and the 6-311++G(d,p) basis set.[34] Vibrational frequencies were computed to confirm the absence of imaginary frequencies and derive zero-point energy and vibrational entropy corrections from unscaled frequencies. Single point energy calculations were performed on the optimized minima using M06-2X/cc-PVTZ.[35] NICS values were calculated using the GIAO method[36] using CAM-B3LYP/6-31+G(d,p) and AICD plots were obtained from CGST calculations using B3LYP/6-31+G(d).[37] NICS(0) was calculated at the mean position of all four heavy atoms in the middle of the macrocycle. NICS(a), NICS(b), NICS(c), NICS(d), NICS(e), NICS(f) and NICS(g) values were obtained by applying the same method to the mean position of the heavy atoms that comprise the individual rings of each macrocycle. In addition, NICS$(1)_{zz}$, NICS$(1a)_{zz}$, NICS$(1b)_{zz}$, NICS$(1c)_{zz}$, NICS$(1d)_{zz}$, NICS$(1e)_{zz}$, NICS$(1f)_{zz}$, and NICS$(1g)_{zz}$ were obtained by applying the same method to ghost atoms placed 1 Å above each of the corresponding NICS(0) points and extracting the *zz* contribution of the magnetic tensor. The resulting energies, Cartesian coordinates, and AICD plots can be found in the Supporting Information.

■ ASSOCIATED CONTENT

Data Availability Statement

The data underlying this study are available in the published article and its online Supporting Information.

Supporting Information

The Supporting Information is available free of charge at https://pubs.acs.org/doi/10.1021/acs.joc.4c01511.

Selected UV−vis (Figures S1−S43), ^{1}H NMR, ^{1}H−^{1}H COSY, HSQC, DEPT-135, ^{13}C{^{1}H} NMR (Figures S44−S109), mass spectra (Figures S110−S115), calculated conformations of selected tautomers (Figure S116−S141), calculated dihedral angles (Tables S1−S7), calculated relative energies (kcal/mol) and NICS values for selected protonated species (Tables S8−S15), calculated Gibbs free energies for optimized structures (Tables S16−S21), AICD plots (Figures S142−S168) and Cartesian coordinates (Table S22) are provided (PDF)

■ AUTHOR INFORMATION

Corresponding Author

Timothy D. Lash − *Department of Chemistry, Illinois State University, Normal, Illinois 61790-4160, United States;* orcid.org/0000-0002-0050-0385; Email: tdlash@ilstu.edu

Authors

Victoria C. Ujah − *Department of Chemistry, Illinois State University, Normal, Illinois 61790-4160, United States*

Deyaa I. AbuSalim − *Department of Chemistry, Illinois State University, Normal, Illinois 61790-4160, United States; Department of Chemistry, Rowan University, Glassboro, New*

Jersey 08028, United States; STEM Department, Rowan College of South Jersey, Vineland, New Jersey 08360, United States

Complete contact information is available at:
https://pubs.acs.org/10.1021/acs.joc.4c01511

Notes

The authors declare no competing financial interest.

■ ACKNOWLEDGMENTS

This work was supported by the National Science Foundation under grants CHE-1855240 and CHE-2247214. NSF is also acknowledged for providing funding for the departmental NMR spectrometers (CHE-0722385) and mass spectrometer (CHE-1337497) under the Major Research Instrumentation (MRI) program.

■ REFERENCES

(1) *The Colours of Life*; Milgrom, L. R., Ed.; Oxford University Press: New York, 1997.

(2) Liu, Y.; Zhang, S.; Lindsey, J. S. Total Synthesis Campaigns Toward Chlorophylls and Related Natural Hydroporphyrins - Diverse Macrocycles, Unrealized Opportunities. *Nat. Prod. Rep.* **2018**, *35*, 879−901.

(3) (a) Rose, E.; Andrioletti, B.; Zrig, S.; Quelquejeu-Ethève, M. Enantioselective Epoxidation of Olefins with Chiral Metalloporphyrin Catalysts. *Chem. Soc. Rev.* **2005**, *34*, 573−583. (b) Lu, H.; Zhang, X. P. Catalytic C-H Functionalization by Metalloporphyrins: Recent Developments and Future Directions. *Chem. Soc. Rev.* **2011**, *40*, 1899−1909. (c) Che, C.-M.; Lo, V. K.-Y.; Zhou, C.-Y.; Huang, J. S. Selective Functionalization of Saturated C-H bonds with Metalloporphyrin Catalysts. *Chem. Soc. Rev.* **2011**, *40*, 1950−1975. (d) Pellissier, H.; Clavier, H. Enantioselective Cobalt-Catalyzed Transformations. *Chem. Rev.* **2014**, *114*, 2775−2823. (e) Gopalaiah, K. Chiral Iron Catalysts for Asymmetric Synthesis. *Chem. Rev.* **2013**, *113*, 3248−3296.

(4) (a) Ding, Y.; Zhu, W.-H.; Xie, Y. Development of Ion Chemosensors Based on Porphyrin Analogues. *Chem. Rev.* **2017**, *117*, 2203−2256. (b) Paolesse, R.; Nardis, S.; Monti, D.; Stefanelli, M.; Di Natale, C. Porphyrinoids for Chemical Sensor Applications. *Chem. Rev.* **2017**, *117*, 2517−2583.

(5) (a) Ono, N.; Ito, S.; Wu, C. H.; Chen, C. H.; Wen, T. C. Nonlinear Light Absorption in *meso*-Substituted Tetrabenzoporphyrin and Tetraarylporphyrin Solutions. *Chem. Phys.* **2000**, *262*, 467−473. (b) Rogers, J. E.; Nguyen, K. A.; Hufnagle, D. C.; McLean, D. G.; Su, W. J.; Gossett, K. M.; Burke, K. M.; Vinogradov, S. A.; Pachter, R.; Fleitz, P. A. Observation and Interpretation of Annulated Porphyrins: Studies on the Photophysical Properties of *meso*-Tetraphenylmetalloporphyrins. *J. Phys. Chem. A* **2003**, *107*, 11331−11339.

(6) Zhang, Y.; Lovell, J. F. Porphyrins as Theranostic Agents from Prehistoric to Modern Times. *Theranostics* **2012**, *2*, 905−915.

(7) (a) Bonnett, R. Photosensitizers of the Porphyrin and Phthalocyanine Series for Photodynamic Therapy. *Chem. Soc. Rev.* **1995**, *24*, 19−33. (b) Ethirajan, M.; Chen, Y.; Joshi, P.; Pandey, R. K. The Role of Porphyrin Chemistry in Tumor Imaging and Photodynamic Therapy. *Chem. Soc. Rev.* **2011**, *40*, 340−362.

(8) (a) Brückner, C.; Akhigbe, J.; Samankumara, L. P.; Smith, K. M.; Kadish, K. M.; Guilard, R. Porphyrin Analogs Containing Non-Pyrrolic Heterocycles. In *Handbook of Porphyrin Science: With Applications to Chemistry, Physics, Material Science, Engineering, Biology and Medicine*; World Scientific: Singapore, 2014; Vol. *31*, pp 1−275. (b) Chatterjee, T.; Shetti, V. S.; Sharma, R.; Ravikanth, M. Heteroatom-Containing Porphyrin Analogues. *Chem. Rev.* **2017**, *117*, 3254−3328. (c) Lash, T. D. Chapter Four—Recent Developments in the Chemistry of Heteroporphyrins and Heterocarbaporphyrins. In *Advances in Heterocyclic Chemistry*; Scriven, E. F. V., Ramsden, C. A., Eds.; Elsevier: Oxford, UK, 2022; Vol. *138*, pp 243−334..

(9) Lash, T. D. Carbaporphyrinoid Systems. *Chem. Rev.* **2017**, *117*, 2313−2446.

(10) Lash, T. D.; Chaney, S. T.; Richter, D. T. Conjugated Macrocycles Related to the Porphyrins. Part 12. Oxybenzi- and Oxypyriporphyrins: Aromaticity and Conjugation in Highly Modified Porphyrinoid Structures. *J. Org. Chem.* **1998**, *63*, 9076−9088.

(11) Stepien, M.; Latos-Grażyński, L.; Szterenberg, L. 22-Hydroxybenziporphyrin: Switching of Antiaromaticity by Keto-Enol Tautomerization. *J. Org. Chem.* **2007**, *72*, 2259−2270.

(12) Lash, T. D.; Chaney, S. T.; Johnson, A. L.; Weisbond, J. T.; Ferrence, G. M. Synthesis, Characterization and Metalation of 22-Hydroxybenziporphyrins. *J. Porphyrins Phthalocyanines* **2021**, *25*, 1095−1103.

(13) Lash, T. D. Modification of the Porphyrin Chromophore by Ring Fusion: Identifying Trends due to Annelation of the Porphyrin Nucleus. *J. Porphyrins Phthalocyanines* **2001**, *5*, 267−288.

(14) Cramer, E. K.; Lash, T. D. Synthesis of a Series of Tropone-fused Porphyrinoids. *J. Org. Chem.* **2022**, *87*, 952−962.

(15) Siri, O.; Jaquinod, L.; Smith, K. M. Coplanar Conjugated β-Nitroporphyrins and Some Aspects of Nitration of Porphyrins with N_2O_4. *Tetrahedron Lett.* **2000**, *41*, 3583−3587.

(16) Ko, M.-S.; Roh, T.-H.; Desale, P. P.; Choi, S.-W.; Cho, D. G. Effects of Electron-Withdrawing and Electron-Donating Groups on Aromaticity in Cyclic Conjugated Polyenes. *J. Am. Chem. Soc.* **2024**, *146*, 6266−6273.

(17) Lin, Y.; Lash, T. D. Porphyrin Synthesis by the "3 + 1" Methodology: A Superior Approach for the Preparation of Porphyrins with Fused 9,10-Phenanthroline Subunits. *Tetrahedron Lett.* **1995**, *36*, 9441−9444.

(18) Lash, T. D.; Lin, Y.; Novak, B. H.; Parikh, M. D. Porphyrins with Exocyclic Rings. Part 19. Efficient Syntheses of Phenanthrolinoporphyrins. *Tetrahedron* **2005**, *61*, 11601−11614.

(19) Okujima, T.; Mifuji, A.; Nakamura, J.; Yamada, H.; Uno, H.; Ono, N. First Synthesis of Porphyrin-fused 1,10-Phenanthroline-Ruthenium(II) Complexes. *Org. Lett.* **2009**, *11*, 4088−4091.

(20) Lash, T. D.; Rauen, P. J. Extended Porphyrinoid Chromophores: Heteroporphyrins Fused to Phenanthrene and Acenaphthylene. *Tetrahedron* **2021**, *100*, 132481.

(21) Saggadi, H.; Luart, D.; Thiebault, N.; Polaert, I.; Estel, L.; Len, C. Quinoline and Phenanthroline Preparation Starting from Glycerol via Improved Microwave-assisted Modified Skraup Reaction. *RSC Adv.* **2014**, *4*, 21456−21464.

(22) Latham, A. N.; Lash, T. D. Synthesis and Characterization of *N*-Methylporphyrins, Heteroporphyrins, Carbaporphyrins, and Related Systems. *J. Org. Chem.* **2020**, *85*, 13050−13068.

(23) *CRC Handbook of Chemistry and Physics*, 97th ed.; Haynes, W. M., Ed.; CRC Press: Boca Raton, 2016; p 3444.

(24) Medforth, C. J. NMR Spectroscopy of Diamagnetic Porphyrins. In *The Porphyrin Handbook*; Kadish, K. M., Smith, K. M., Guilard, R., Eds.; Academic Press: San Diego, 2000; Vol. *5*, pp 1−80.

(25) Wu, J. I.; Fernandez, I.; Schleyer, P. v. R. Description of Aromaticity in Porphyrinoids. *J. Am. Chem. Soc.* **2013**, *135*, 315−321.

(26) Ghosh, A. First-Principles Quantum Chemical Studies of Porphyrins. *Acc. Chem. Res.* **1998**, *31*, 189−198.

(27) Aihara, J.-i.; Nakagami, Y.; Sekine, R.; Makino, M. Validity and Limitations of the Bridged Annulene Model for Porphyrins. *J. Phys. Chem. A* **2012**, *116*, 11718−11730.

(28) Valiev, R. R.; Fliegl, H.; Sundholm, D. Predicting the Degree of Aromaticity of Novel Carbaporphyrinoids. *Phys. Chem. Chem. Phys.* **2015**, *17*, 14215−14222.

(29) Schleyer, P. v. R.; Maerker, C.; Dransfeld, A.; Jiao, H.; van Eikema Hommes, N. J. R. Nucleus-Independent Chemical Shifts: a Simple and Efficient Aromaticity Probe. *J. Am. Chem. Soc.* **1996**, *118*, 6317−6318.

(30) Geuenich, D.; Hess, K.; Köhler, F.; Herges, R. Anisotropy of Induced Current Density (ACID), a General Method to Quantify and Visualize Electronic Delocalization. *Chem. Rev.* **2005**, *105*, 3758−3772.

(31) Arnold, Z. Synthetic Reactions of Dimethylformamide. XXII. Formation and Preparation of Formyl Derivatives of Indene. *Collect. Czech. Chem. Commun.* **1965**, *30*, 2783−2792.

(32) Lash, T. D.; Hayes, M. J.; Spence, J. D.; Muckey, M. A.; Ferrence, G. M.; Szczepura, L. F. Conjugated Macrocycles Related to the Porphyrins. Part 21. Synthesis, Spectroscopy, Electrochemistry and Structural Characterization of Carbaporphyrins. *J. Org. Chem.* **2002**, *67*, 4860−4874.

(33) Frisch, M. J.; Trucks, G. W.; Schlegel, H. B.; Scuseria, G. E.; Robb, M. A.; Cheeseman, J. R.; Scalmani, G.; Barone, V.; Petersson, G. A.; Nakatsuji, H.; Li, X.; Caricato, M.; Marenich, A. V.; Bloino, J.; Janesko, B. G.; Gomperts, R.; Mennucci, B.; Hratchian, H. P.; Ortiz, J. V.; Izmaylov, A. F.; Sonnenberg, J. L.; Williams-Young, D.; Ding, F.; Lipparini, F.; Egidi, F.; Goings, J.; Peng, B.; Petrone, A.; Henderson, T.; Ranasinghe, D.; Zakrzewski, V. G.; Gao, J.; Rega, N.; Zheng, G.; Liang, W.; Hada, M.; Ehara, M.; Toyota, K.; Fukuda, R.; Hasegawa, J.; Ishida, M.; Nakajima, T.; Honda, Y.; Kitao, O.; Nakai, H.; Vreven, T.; Throssell, K.; Montgomery, J. A., Jr.; Peralta, J. E.; Ogliaro, F.; Bearpark, M. J.; Heyd, J. J.; Brothers, E. N.; Kudin, K. N.; Staroverov, V. N.; Keith, T. A.; Kobayashi, R.; Normand, J.; Raghavachari, K.; Rendell, A. P.; Burant, J. C.; Iyengar, S. S.; Tomasi, J.; Cossi, M.; Millam, J. M.; Klene, M.; Adamo, C.; Cammi, R.; Ochterski, J. W.; Martin, R. L.; Morokuma, K.; Farkas, O.; Foresman, J. B.; Fox, D. J. *Gaussian 16*. revision C.01; Gaussian, Inc.: Wallingford, CT, 2019.

(34) (a) Clark, T.; Chandrasekhar, J.; Spitznagel, G. W.; Schleyer, R. v. P. Efficient Diffuse Function-augmented Basis Sets for Anion Calculations. III. The 3-21+G Basis Set for First-Row Elements, Li-F. *J. Comput. Chem.* **1983**, *4*, 294−301. (b) Ditchfield, R.; Hehre, W. J.; Pople, J. A. Self-Consistent Molecular-Orbital Methods. IX. An Extended Gaussian-Type Basis for Molecular-Orbital Studies of Organic Molecules. *J. Chem. Phys.* **1971**, *54*, 724−728. (c) Hariharan, P. C.; Pople, J. A. The Influence of Polarization Functions on Molecular Orbital Hydrogenation Energies. *Theor. Chim. Acta* **1973**, *28*, 213−222. (d) Hehre, W. J.; Ditchfield, R.; Pople, J. A. Self-Consistent Molecular Orbital Methods. XII. Further Extensions of Gaussian-Type Basis Sets for Use in Molecular Orbital Studies of Organic Molecules. *J. Chem. Phys.* **1972**, *56*, 2257−2261.

(35) Dunning, T. H., Jr. Gaussian Basis Sets for use in Correlated Molecular Calculations. I. The Atoms Boron through Neon and Hydrogen. *J. Chem. Phys.* **1989**, *90*, 1007−1023.

(36) Chen, Z.; Wannere, C. S.; Corminboeuf, C.; Puchta, R.; Schleyer, P. v. R. Nucleus-Independent Chemical Shifts (NICS) as an Aromaticity Criterion. *Chem. Rev.* **2005**, *105*, 3842−3888.

(37) Herges, R.; Geuenich, D. Delocalization of Electrons in Molecules. *J. Phys. Chem. A* **2001**, *105*, 3214−3220.